Therapeutic mechanisms of high-frequency stimulation in Parkinson's disease and neural restoration via loop-based reinforcement

Sabato Santaniello[a,1,2], Michelle M. McCarthy[b], Erwin B. Montgomery Jr.[c], John T. Gale[d,e], Nancy Kopell[b], and Sridevi V. Sarma[a,f]

[a]Institute for Computational Medicine and [f]Department of Biomedical Engineering, The Johns Hopkins University, Baltimore, MD 21218; [b]Department of Mathematics and Statistics, Boston University, Boston, MA 02215; [c]Greenville Neuromodulation Center, Greenville, PA 16125; and [d]Department of Neuroscience, Lerner Research Institute and [e]Center for Neurological Restoration, Neurological Institute, Cleveland Clinic, Cleveland, OH 44195

Edited by Terrence J. Sejnowski, Salk Institute for Biological Studies, La Jolla, CA, and approved September 26, 2014 (received for review April 9, 2014)

High-frequency deep brain stimulation (HFS) is clinically recognized to treat parkinsonian movement disorders, but its mechanisms remain elusive. Current hypotheses suggest that the therapeutic merit of HFS stems from increasing the regularity of the firing patterns in the basal ganglia (BG). Although this is consistent with experiments in humans and animal models of Parkinsonism, it is unclear how the pattern regularization would originate from HFS. To address this question, we built a computational model of the cortico-BG-thalamo-cortical loop in normal and parkinsonian conditions. We simulated the effects of subthalamic deep brain stimulation both proximally to the stimulation site and distally through orthodromic and antidromic mechanisms for several stimulation frequencies (20–180 Hz) and, correspondingly, we studied the evolution of the firing patterns in the loop. The model closely reproduced experimental evidence for each structure in the loop and showed that neither the proximal effects nor the distal effects individually account for the observed pattern changes, whereas the combined impact of these effects increases with the stimulation frequency and becomes significant for HFS. Perturbations evoked proximally and distally propagate along the loop, rendezvous in the striatum, and, for HFS, positively overlap (reinforcement), thus causing larger poststimulus activation and more regular patterns in striatum. Reinforcement is maximal for the clinically relevant 130-Hz stimulation and restores a more normal activity in the nuclei downstream. These results suggest that reinforcement may be pivotal to achieve pattern regularization and restore the neural activity in the nuclei downstream and may stem from frequency-selective resonant properties of the loop.

deep brain stimulation | Parkinson's disease | basal ganglia | thalamus | reinforcement

High-frequency (i.e., above 100 Hz) deep brain stimulation (HFS) of the basal ganglia (BG) and thalamus is clinically recognized to treat movement disorders in Parkinson's disease (PD) (1–4), but its therapeutic mechanisms remain unclear (5, 6).

Early hypotheses about HFS were derived from the rate-based model of the BG function (7, 8) and postulated the disruption of the output of the BG-thalamic system via either the inactivation of neurons in the stimulated site (target) (9–15), which would provide an effect similar to a surgical lesion, or the abnormal excitation of axons projecting out of the target (16–19), which would disrupt the neuronal activity in the structures downstream, including any pathophysiological activity (20).

More recently, an ever-growing number of experiments in PD humans and animal models of Parkinsonism has indicated that HFS affects the firing patterns of the neurons rather than the mean firing rate both in the target and the structures downstream (18, 19, 21–31) and it replaces repetitive low-frequency (i.e., ≤50 Hz) bursting patterns with regularized (i.e., more tonic) patterns at higher frequencies (25, 26). It has been proposed that increased pattern regularity of neurons in the target may be therapeutic (5, 32–37), but it is still unknown how this regularity comes about with HFS.

It has been suggested that an increased pattern regularity can deplete the information content of the target output and this lack of information would act as an "information lesion" (33) and prevent the pathological activity from being transmitted within the BG-thalamic system (22, 33, 36). As a result, an information lesion in the target [typically, one among the subthalamic nucleus (STN), internal globus pallidus (GPi), or thalamus] would have effects similar to those of a destructive lesion in the same site, which has been reported to alleviate the movement disorders (38).

Instead, studies (32, 34, 35, 37) have suggested that an increased pattern regularity of the BG output partly compensates the PD-evoked impairment of the information-processing capabilities of the thalamo-cortical system, and this restores a more faithful thalamic relay of the sensorimotor information (35, 39).

Although intriguing, these hypotheses remain elusive on (*i*) the neuronal mechanisms that would elicit pattern regularization (e.g., why regularization would be relevant only for HFS) and (*ii*) the effects that increased regularity would have on the cortico-BG-thalamo-cortical loop.

It has been hypothesized that pattern regularization occurs because axons projecting out of the target follow the pattern of the stimulus pulses (40, 41) and, given the segregated organization of the BG-thalamic connections (42), it has been assumed

Significance

We investigated the therapeutic mechanisms of high-frequency stimulation (HFS) in Parkinson's disease by developing a computational model of the cortico-basal ganglia-thalamo-cortical loop in normal and parkinsonian conditions under the effects of stimulation at several frequencies. We found that the stimulation injected in the loop elicits neural perturbations that travel along multiple pathways with different latencies and rendezvous in striatum (one of the basal ganglia). If the stimulation frequency is high enough, these perturbations overlap (reinforcement) and cause more regular, stimulus-locked firing patterns in striatum. Overlap is maximal at clinically relevant HFS and restores more normal activity in the remaining structures of the loop. This suggests that neural restoration and striatal reinforcement may be a therapeutic merit and mechanism of HFS, respectively.

Author contributions: S.S. and S.V.S. designed research; S.S. performed research; S.S. analyzed data; and S.S., M.M.M., E.B.M., J.T.G., N.K., and S.V.S. wrote the paper.

The authors declare no conflict of interest.

This article is a PNAS Direct Submission.

[1]Present address: Department of Biomedical Engineering, University of Connecticut, Storrs, CT 06269.

[2]To whom correspondence should be addressed. Email: sabato@engr.uconn.edu.

This article contains supporting information online at www.pnas.org/lookup/suppl/doi:10.1073/pnas.1406549111/-/DCSupplemental.

that pattern regularization percolates straightforward from the target to the structures immediately downstream (34, 36). However, this representation of the pattern regularization as a "local" effect can hardly be reconciled with the fact that HFS of any structure of the cortico-BG-thalamo-cortical loop is therapeutic for at least some movement disorders (1–4, 43–47), nor does it explain why stimulation at frequencies above 160–180 Hz is not necessarily therapeutic despite the fact that the regularity of the axonal patterns may increase (48, 49). Moreover, coherence in the 8–30-Hz band among neurons across different structures may decrease under HFS but not for lower frequencies (26, 50–52), which suggests the emergence of diffused changes in neuronal activity that would be hardly accounted for with purely local effects.

There is emerging evidence, instead, that HFS affects multiple structures simultaneously. First, it has been shown that deep brain stimulation (DBS) may antidromically activate afferent axons and fibers of passage (53–59), thus reaching structures not immediately downstream. Second, studies (57, 58) observed in 6-hydroxydopamine (6-OHDA)-intoxicated rats that the antidromic effects increase with the stimulation frequency and peak around 110–130 Hz. Third, it has been shown in 1-methyl-4-phenyl-1,2,3,6-tetrahydropyridine (MPTP)-intoxicated nonhuman primates (NHPs) that STN DBS may evoke similar poststimulus responses in different BG structures, both downstream from and upstream to the STN (5, 27, 28, 30, 60). Finally, it has been reported that the cortico-BG-thalamo-cortical system consists of multiple sets of reentrant, interconnected, and partially overlapping neuronal loops (5, 42, 61, 62), which means that the structures upstream to the target (e.g., the striatum) may play an important role in the therapeutic mechanisms of HFS.

Altogether, these results suggest that (A) pattern regularization is a global effect that exploits the closed-loop nature of the cortico-BG-thalamo-cortical system and selectively emerges only for specific HFS values, and that (B) the therapeutic merit of pattern regularization has to deal with the restoration of a more normal functionality of the entire cortico-BG-thalamo-cortical loop rather than with variations in the information content of one specific structure.

We explored hypotheses (A) and (B) and assessed the system-wide effects of DBS by constructing a computational model of the cortico-BG-thalamo-cortical loop in both normal and parkinsonian conditions and by simulating the effects of STN DBS both at low (20–80 Hz) and high (100–180 Hz) frequencies. The model includes populations of single-compartment neurons and interneurons from motor cortex, striatum, GPi, and thalamus according to a network topology derived from the NHP anatomy, and it simulates both the orthodromic and antidromic effects of DBS. As a result, this model reproduced both average activity and discharge patterns of single units in NHP and rats under normal and parkinsonian conditions, with and without DBS, for all modeled structures.

We show through numerical simulation that hypothesis (A) is significantly contributed by reinforcement mechanisms in the striatum. These mechanisms are selectively elicited by HFS, facilitate the percolation of regularized discharge patterns from the striatum to the GPi, and have a primary role in (B), because the percolated striato-pallidal input combines with the local effects of STN DBS to restore the thalamic relay function (63).

Results

We modeled the "direct pathway" in the cortico-BG-thalamo-cortical loop (7, 8) (a schematic is shown in Fig. S1) by using single-compartment neurons from the motor cortex [200 pyramidal neurons (PYNs) and 20 fast-spiking interneurons (FSIs)], dorsolateral striatum [i.e., putamen, 200 medium spiny neurons (MSNs) and 20 parvalbumin-positive interneurons (PPIs)], GPi [200 pallidal neurons (PANs)], and ventrolateral thalamus [200 thalamocortical neurons (TCNs) and 40 reticular neurons (RENs)].

The activity of the remaining BG nuclei was subsumed in the input delivered to the GPi neurons and it varied in normal and PD conditions (64). The connections between neurons were chosen consistently with the neuronal anatomy in NHPs and the synaptic conductances were randomized across the entire network to increase the pattern variability of the neurons at rest (*SI Notes 1* and *2*).

DBS in the subthalamic area may elicit direct effects on the GPi [monosynaptic orthodromic activation (17)], putamen [both monosynaptic orthodromic activation and antidromic activation of striatonigral projections (5, 65–67)], cortex [antidromic activation of cortico-subthalamic projections (53, 56–58)], and thalamus [antidromic activation of cortico-subthalamic collaterals to the thalamus (31)]. We simulated these effects by applying a delayed depolarizing current pulse for each DBS pulse to the PANs, MSNs, PYNs, and TCNs. The lag between current pulses and DBS input varied according to the depolarization mechanism (orthodromic vs. antidromic) and structure, and the pulse amplitudes were randomly distributed to simulate the stochastic effects of both antidromic and orthodromic propagation (17, 18, 58) (Fig. S2 and *SI Note 3*).

Regular DBS (i.e., constant interpulse interval) was applied at 20, 50, 80, 100, 130, 160, and 180 Hz. Nonregular DBS (i.e., interpulse intervals following a gamma distribution; *SI Note 3*) with average frequency of 130 Hz was also applied. For each combination of disease condition and DBS setting, three instances of the model were generated and each instance was simulated for 32,000 ms. The first 2,000 ms of each simulation were neglected to let the model reach steady-state conditions and results were averaged across the model instances.

Normal vs. Parkinsonian Conditions at Rest. Figs. 1–5 report the population-averaged results for the projecting neurons in the GPi (PANs), putamen (MSNs), cortex (PYNs), and thalamus (TCNs), respectively, under normal and PD conditions at rest. Each population was $N = 600$ neurons (i.e., total number of neurons across three model instances). The multifarious effects of the PD-elicited loss of dopamine on the $D_{1–5}$ dopaminergic receptors on the MSNs and on the interneurons in the putamen (68) were simulated by varying the maximal conductance of the M-type potassium currents in the MSNs and the activity of the PPIs. We also changed the stochastic distribution of the inputs delivered to the GPi neurons, thus simulating the effects of the loss of dopamine on the GPe–STN subsystem (*SI Note 2*).

As a result, the simulated PANs showed a 56% increment of the population-averaged pairwise cross-correlation at the transition from normal to PD conditions (*SI Note 4* and *5*), 26% increment in the average firing rate (Fig. 1*E*), and an increased incidence of the bursting mode, thus reproducing experimental results in refs. 17 and 69–71 for NHPs. A comparison between simulated and actual NHP single units from ref. 17 is reported in Fig. 1 *A* and *C*.

The percentage of time spent by PANs in bursts raised from 9.1 ± 2.3% (normal) to 22.3 ± 4.0% (PD), the percentage of GPi spikes belonging to bursts raised from 13.9 ± 3.4% to 58.5 ± 16.0% (mean ± S.D.), and the population-average rates (firing and burst rate) were comparable to the values in refs. 17, 23, and 71 for both normal and MPTP-treated NHPs (Fig. 1 *E* and *F*). Furthermore, the spectral analysis of the spiking patterns showed that, under PD conditions, the PANs had exaggerated oscillations either in the 4- to 8-Hz band (tremor band, 60% of the population) or in the 10- to 15-Hz band (beta band, 40% of the population), Fig. 2 *A* and *B*. These oscillations were caused by a combination of the input from putamen (72) and the input from the GPe–STN subsystem (73). The frequency bands of the oscillations and the ratio between the number of neurons with tremor- and beta-band oscillations were consistent with experiments in refs. 51, 52, 69, and 70 (Fig. 2*C*).

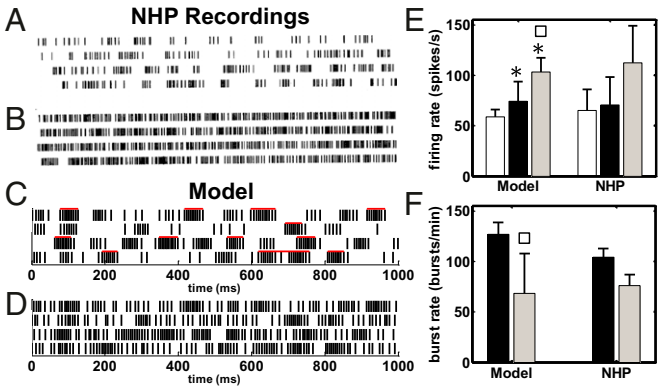

Fig. 1. (*A–D*) Raster plot of a GPi neuron under PD conditions at rest (*A* and *C*) and with STN HFS (*B* and *D*). *A* and *B* are from an MPTP-treated NHP (modified with permission from ref. 17). *C* and *D* are from a pallidal neuron in our model. Red bars in *C* denote estimated bursts. (*E*) Population-average firing rate (mean ± SD) of the GPi neurons under normal (white), PD (black), and PD with STN HFS (PD+HFS, gray) conditions in our model and NHPs. (*F*) Population-average burst rate (mean ± SD) of the GPi neurons under PD (black) and PD+HFS (gray) conditions in our model and NHPs. Population-average burst rate of the GPi under normal condition is 20.9 ± 4.7 bursts per minute (mean ± SD). Rates for NHPs in *E* and *F* are reported in refs. 17 and 71 and ref. 23, respectively. Asterisks (squares) show significant differences normal vs. PD and PD+HFS (PD vs. PD+HFS), one-way ANOVA with Tukey–Kramer post hoc test, $P < 0.001$. HFS is 136 Hz in the NHPs (*B*, *E*, and *F*) and 130 Hz in our model (*D–F*).

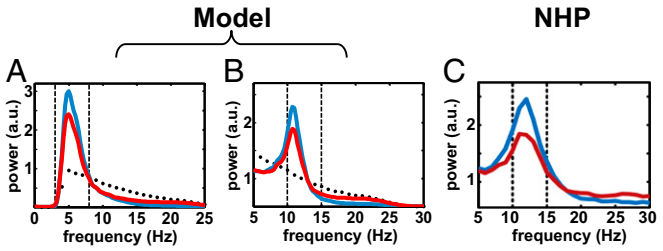

Fig. 2. (*A* and *B*) Population-average normalized power spectrum density (PSD) of tremor-band-oscillatory (*A*) and beta-band-oscillatory (*B*) GPi neurons in our model under normal (black dots), PD (blue line), and PD+HFS (red line) conditions. (*C*) Population-average normalized PSD of beta-band-oscillatory GPi neurons from a NHP under PD (blue line) and PD+HFS (red line) conditions. HFS is 130 Hz in *A* and *B* and 125 Hz in *C*. *C* is modified with permission from ref. 51.

Under PD conditions, the modulation of M-type potassium currents and the reduced GABAergic input from the striatal interneurons affected the activity of the MSNs. Overall, 72% of the MSNs (490 out of 600) increased the average firing rate (*t* test, $P < 0.05$), which is consistent with refs. 74 and 75, whereas the remaining neurons decreased it. As a result, even though the mean firing rate increased, there was a larger variability of the spiking patterns across the population (Fig. 3 *A* and *B*) and an increased level of pairwise cross-correlation (*SI Note 5*).

Overall, the changes in the striato-pallidal subsystem had minor effects on the average activity of the cortical and thalamic neurons. In cortex, the percentage of PYNs with random, regular, or bursty patterns mildly changed at the transition from normal to PD conditions (random: 270 vs. 290; regular: 97 vs. 121; bursty: 231 vs. 184; normal vs. PD; definition of the patterns is given in ref. 76 and *SI Note 4*), and nonsignificant changes (Wilcoxon rank-sum test, $P > 0.05$) were reported for the distribution of the firing rates across the PYNs (Fig. 4 *A*, *B*, *D*, and *E*), the population-average firing rate (Fig. 4*C*), and the percentage of time spent in burst activity (Fig. 4*F*), consistently with ref. 76 (M1 group). We measured the fraction of power allocated in the 8–30-Hz band for each PYN and we found that this fraction increased in 331 out of 600 PYNs when under PD conditions, which is consistent with the increment of oscillations in that band reported by ref. 76. The average increment in the 8–30 Hz power across these 331 PYNs was 5.9 ± 6.0% (mean ± SD, range: 0–53.9%) and resulted in no prominent oscillation in that band, which is consistent with the analysis of single unit recordings of MPTP-treated NHPs reported in ref. 52.

Analogously, the sample distribution of the mean firing rates across the population of TCNs was similar in normal and PD conditions and reproduced experimental results in refs. 77–79 for nontremulous NHPs (Fig. 5 *A*, *B*, *D*, and *E*). Moreover, the majority of TCNs preserved a random discharge pattern and the number of bursty TCNs remained small across the disease conditions, whereas the number of regular TCNs decreased (random, bursty, and regular pattern: 471 vs. 527, 51 vs. 32, and 70 vs. 41 TCNs, respectively, normal vs. PD conditions), consistently with the trend reported in ref. 78. On the other hand, the loss of dopamine had an effect on the oscillations of the TCN discharge pattern: 224 out of 600 TCNs had a significant change in the interspike interval (ISI) histogram (*t* test, $P < 0.05$), with an enhanced bimodal distribution of the ISIs in PD conditions and peaks around 3 ms and 30 ms (Fig. 6 *A* and *B*), consistently with data from MPTP-treated NHPs (31). Correspondingly, the difference between the power spectrum of the spike trains under normal and PD conditions [mean square error (MSE) in the 3–100-Hz band] was significant (Fig. 7*A*, $P < 0.001$).

Direct Effects of STN DBS on the GPi, Thalamus, Cortex, and Putamen. STN DBS at 130 Hz (range: 125–136 Hz) has been reported to restore movement disorders in MPTP-treated NHPs and 6-OHDA–treated rats (5, 15, 17, 23, 28, 31, 51, 57, 80).

In our model under PD conditions, 130-Hz STN DBS affected the GPi PANs by inducing more regular firing patterns, higher average firing rates, and lower burstiness (Fig. 1 *B*, *E*, and *F*), with results matching experimental observations in refs. 17 and 23 (Fig. 1 *D–F*). The percentage of time spent in bursts and the percentage of spikes belonging to bursts dropped to 14.8 ± 6.7% and 27.7 ± 15.5% (mean ± SD), respectively, and the oscillations in the tremor and beta band were significantly attenuated (Wilcoxon rank-sum test, $P < 0.001$), consistently with results in ref. 51 (Fig. 2).

STN DBS at 130 Hz also affected the remaining structures in the model under PD conditions. The population-average firing rate significantly increased (*t* test, $P < 0.001$) for the MSNs (Fig. 3 *C* and *D*) and PYNs (Fig. S3) and it mildly decreased for the TCNs (Fig. 5 *C* and *F*), whereas individual TCNs either significantly increased (77 out of 600) or decreased (339 out of 600) the firing rate (*t* test, $P < 0.05$), consistently with experiments in refs. 31, 57, and 80. Furthermore, the ISI histogram for the TCNs moved from a continuous distribution to a multimodal distribution with peaks corresponding to multiples of the DBS interpulse interval (Fig. 6 *A* and *B*), whereas the spectral content of the TCN spike trains was affected in a way that compensated for the changes induced by the PD conditions and returned to a value close to normal conditions (MSE was minimal and ≅ 0, Fig. 7*A*).

The firing pattern of the TCNs, however, remained significantly different from normal when 130-Hz STN DBS was applied. These neurons tended to fire an action potential with short latency (1–2 ms) after each DBS pulse [z-score >2.58, which corresponds to a *P* value $P < 0.01$ (18)] as in ref. 31 (Fig. 6 *C* and *D*) and were entrained to similar patterns, as suggested by the fact that ∼80% of the TCNs were likely to fire a poststimulus action potential with the same latency (Fig. S4*B*). The population-average pairwise cross-correlation, instead, decreased by 16.7% and was similar to the normal case (less than 1% difference, *SI Note 5*).

Analogously to the TCNs, PYNs in the cortex, PANs in the GPi, and MSNs in the putamen were consistent with single unit

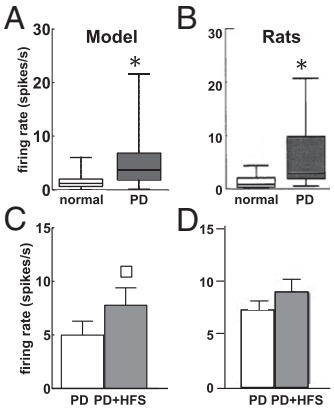

Fig. 3. (*A* and *B*) Box plots of the firing rate of MSNs in our model (*A*) and in Sprague–Dawley rats (*B*) under normal (white) and PD (gray) conditions. In each box plot, the median value (black line), 25th and 75th percentiles (bar limits), and 10th and 90th percentiles (error bars) are shown. (*C* and *D*) Population-average firing rate (mean ± SD) of the MSNs in our model (*C*) and Sprague–Dawley rats (*D*) under PD conditions (white) and PD with 130-Hz STN DBS (PD+HFS, gray). Asterisks in *A* and *B* and square in *C* denote significant differences (Wilcoxon rank-sum test, $P < 0.001$). *B* and *D* are modified with permission from refs. 75 and 80, respectively.

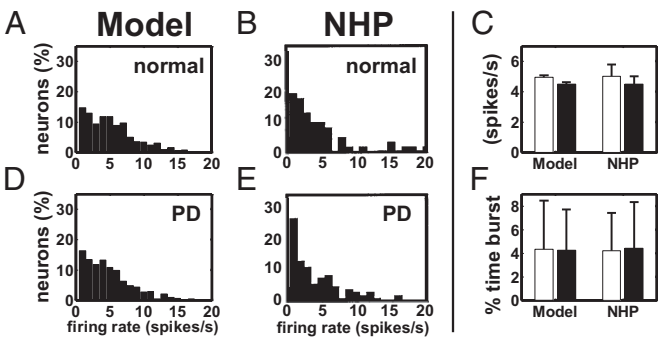

Fig. 4. Histograms of single unit mean firing rates under normal (*A* and *B*) and PD (*D* and *E*) conditions for the PYNs in our model (*A* and *D*) and in the M1 cortex of a NHP (*B* and *E*). (*C*) Population-average firing rate (mean ± SEM) of the PYNs in normal (white) and PD (black) conditions in our model and in the M1 cortex of an NHP. (*F*) Population-average percentage of time (mean ± SD) spent by PYNs in bursts in our model and in the M1 cortex of an NHP. Data for NHPs in *C* and *F* are reported in refs. 102 (animal Z) and 76, respectively. Histograms in *B* and *E* are modified with permission from ref. 102.

recordings in refs. 5, 28, 30, 57, and 58, i.e., they showed a patterned poststimulus response and an increased likelihood of firing action potentials with short latency after each DBS pulse (Fig. 8), despite the fact that the average firing rate remained significantly lower than the DBS frequency (Fig. S3).

These results were determined by a combination of low stimulation efficacy and distal effects. As in refs. 18 and 57, we focused on each structure and we measured the DBS efficacy as the fraction of STN DBS pulses that result into a poststimulus spike of the neurons in that structure. We found that, for the given amplitudes of the DBS-evoked postsynaptic currents (*SI Note 3*), only 35% of the DBS pulses at 130 Hz elicited a poststimulus spike in the pallidal neurons and only 3.5–6.8% elicited a spike in TCNs, PYNs, or MSNs, thus limiting the increase of the average firing rate. Nonetheless, the poststimulus currents to the cortex, thalamus, and putamen were pivotal to achieve the early (i.e., latency of 1–2 ms) poststimulus excitation in Fig. 6 *C* and *D* and Fig. 8 (compare with Fig. S5, where these currents were blocked), thus indicating that the distal effects of STN DBS (i.e., the antidromic activation of cortico-subthalamic projections, orthodromic activation of cortico-thalamic collaterals of these cortico-subthalamic projections, orthodromic activation of subthalamo-striatal projections, and antidromic activation of the striatonigral projections) are pivotal to the overall change in pattern reported in the BG structures.

STN HFS Elicits Thalamic Restoration. We tested several DBS frequencies in the range 20–180 Hz on our model under PD conditions and we assessed the effect of stimulation on the thalamic activity (Fig. 7). Compared with the rest conditions, the spectral MSE for the TCNs either increased or did not significantly change for nontherapeutic DBS (20–100 Hz), whereas it dropped for DBS above 100 Hz (Kruskal–Wallis test with Tukey–Kramer post hoc test, $P < 0.001$) (Fig. 7*A*).

Correspondingly, we assessed the fidelity of the TCNs in relaying cortical inputs (63), which has been proposed in refs. 34 and 35 as a measure of the restoration of the normal thalamic function. We found that the amount of misresponses to the cortical inputs (fidelity loss, see definition in *SI Note 4*) increased under PD conditions and this increment was worsened by low-frequency DBS (20–50 Hz) and mildly compensated by nontherapeutic DBS (80–100 Hz), which indicate an overall deterioration of the relay performance (Fig. 7*B*). Instead, the loss in fidelity was significantly reduced for DBS at frequencies above 100 Hz (Kruskal–Wallis test with Tukey–Kramer post hoc test, $P < 0.001$) and achieved values ≅ 0, thus indicating a restoration of the normal thalamic relay performance. Interestingly, the restoration of the spectral activity and the thalamic performance required both the regularity of the DBS input and the contribution of the distal effects of STN DBS. To prove this, we compared the spectral MSE for the TCNs (Fig. 7*C*) and the loss in fidelity (Fig. 7*D*) caused by PD conditions under no DBS (PD in Fig. 7 *C* and *D*), regular 130-Hz STN DBS (F and D), and irregular 130-Hz STN DBS (R). For settings R, the DBS input was a memoryless point process with instantaneous rate following a gamma function (130 ± 78 Hz, mean ± SD; *SI Note 3* and ref. 36), whereas settings D and F included the subthalamopallidal orthodromic effects of DBS on the GPi only (D) and both the orthodromic and antidromic effects of DBS on the GPi, cortex, putamen, and thalamus (F), respectively. Fig. 7 *C* and *D* shows that both the MSE and the loss in fidelity were minimal and close to 0 (i.e., the normal conditions were restored, $P < 0.01$) only in settings F, whereas both the lack of the antidromic effects (D) and the lack of DBS regularity (R) were unable to compensate the effects caused by the PD conditions.

Striatal Reinforcement As a Mechanism of HFS-Elicited Thalamic Restoration. Fig. 7 indicates that any DBS frequency above 100 Hz can produce some level of compensation of the effects of PD on the thalamic function but results are maximized for 130-Hz DBS. Hence, we hypothesized that this frequency selectivity depends on the closed-loop nature of the cortico-BG-thalamo-cortical system and the overlap of several pathways in the striatum (Fig. S1).

We analyzed the firing pattern of the MSNs in our model under PD conditions and STN DBS by constructing the bi-PSTH (poststimulus time histogram) for several DBS frequencies (Fig. 9). Differently from the PSTH (Fig. 6 *C* and *D* and Fig. 8), which estimates the likelihood of poststimulus spikes normalized to the prestimulation activity (18), the bi-PSTH is a 2D histogram whose generic element (x,y) focuses on two consecutive DBS pulses and estimates the likelihood that the first spike after the first pulse and the first spike after the second pulse occur with latency of x and y ms, respectively (*SI Note 4*), thus estimating the dispersion of the poststimulus latencies across consecutive DBS pulses and assessing the entrainment of the pattern to DBS.

We found that the latencies were highly dispersed for low-frequency DBS and nonsignificantly different from the baseline

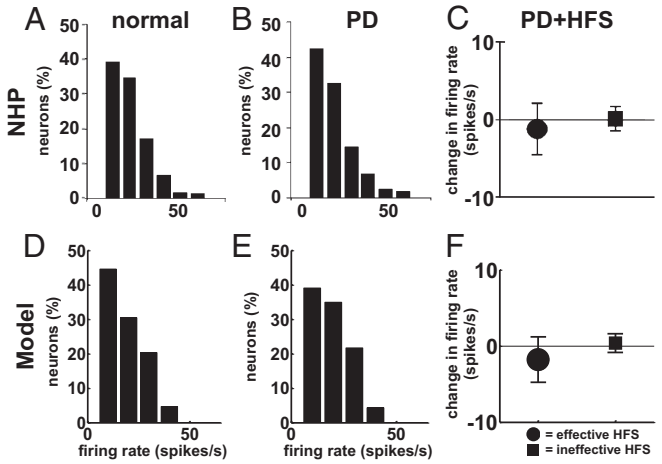

Fig. 5. Firing rate of TCNs in the ventrolateral thalamus of NHPs (*A*–*C*) and in our model (*D*–*F*) under normal, PD, and PD with STN HFS (PD+HFS) conditions. (*A*, *B*, *D*, and *E*) Histograms of mean firing rates under normal (*A* and *D*) and PD (*B* and *E*) conditions at rest. (*C* and *F*) Population-average (mean ± SD) variation of the firing rate of the TCNs at the transition from PD to PD+HFS conditions when the amplitude of the DBS pulses is therapeutically effective (circles) or ineffective (squares) (*SI Note 3*). STN HFS is 136 Hz in *C* and 130 Hz in *F*. *A* and *B* are modified with permission from ref. 78, and *C* is modified from permission from ref. 31.

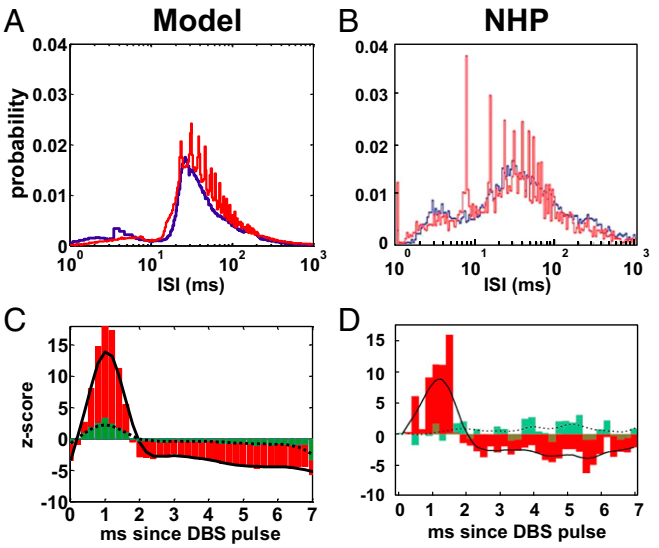

Fig. 6. (*A* and *B*) ISI histogram of the TCNs in our model under PD conditions (*A*) and in a MPTP-treated NHP (*B*) at rest (i.e., no DBS applied, blue lines) and under effective STN HFS (red lines). (*C* and *D*) Population-averaged PSTH of the TCNs in *A* (*C*) and *B* (*D*), respectively, for effective STN HFS. HFS is 130 Hz in *A* and *C* and 136 Hz in *B* and *D*. Red bars and black line in *C* and *D* indicate the PSTH (bin: 0.2 ms) and its envelope (i.e., a smoothing running average of the PSTH), respectively, for effective HFS. Green bars and dotted line in *C* and *D* indicate the PSTH and its envelope, respectively, for ineffective HFS. Definition of "effective" and "ineffective" HFS is in ref. 31. *B* and *D* are reproduced with permission from ref. 31.

prestimulation condition (Fig. 9 *A* and *B*), whereas for high-frequency DBS (*i*) the firing pattern was characterized by a small set of latencies, (*ii*) all these latencies were close to the propagation latency of the DBS pulses toward the MSNs (Fig. S2), and (*iii*) the neurons were entrained to the DBS input (Fig. 9 *C* and *D*).

Unlike for the other high-frequency values we noted that for 130-Hz DBS the range of paired latencies (x,y) with significant likelihood ($P<0.001$) was minimal. The average z-score, instead, was maximal and significantly different from the z-score estimated for the other DBS frequencies (Fig. 9*E*, one-way ANOVA with Tukey–Kramer post hoc test, $P<0.001$), thus indicating that the level of entrainment was overall maximized.

To assess whether the entrainment was just an effect of the DBS-elicited direct input to the MSNs (i.e., I_{DBS} in Fig. S2), we measured the population-average latency of the first poststimulus spike (Fig. 9*F*). Results indicate that the latency decreased monotonically with the DBS frequency and plateaued at the value of the propagation latency of the direct effects of DBS, presumably because the number of DBS inputs I_{DBS} increases with the DBS frequency while the duration of interpulse intervals decreases. The entrainment, instead, occurs if distinct neurons respond with similar latencies and discharge patterns to a common subthreshold input. Typically, this is a consequence of an increased level of excitability of the neurons (i.e., higher subthreshold membrane voltage), which may actually enhance the effects of low-amplitude currents I_{DBS} and make the poststimulus latencies more uniform.

We investigated the origins of the increased excitability of the MSNs by assessing the timing of the PYNs and TCNs that project on the MSNs. In particular, we inquired whether the excitability was just a consequence of the increased firing rate of the cortical input to the MSNs or rather an effect of the percolation of DBS stimuli through the pallido-thalamo-striatal and pallido-thalamo-cortico-striatal pathways (Fig. S1). To this purpose, we applied irregular 130-Hz STN DBS (as for settings R in Fig. 7 *C* and *D*) and we found that, despite the fact that the average firing rate of the cortical and thalamic neurons was higher for irregular than regular 130-Hz DBS (PYNs: 10.5 ± 4.3 Hz vs. 8.9 ± 4.5 Hz; TCNs: 16.3 ± 11.6 Hz vs. 12.4 ± 11.3 Hz; *t* test, $P<0.001$), the average z-score of the bi-PSTH of the MSNs was lower ($P<0.001$) and the range of poststimulus latencies was larger (4.95 ± 7.49 ms vs. 3.69 ± 1.98 ms, $P<0.001$). Overall this indicates that the excitability of the MSNs and their entrainment to the DBS input were inferior for irregular DBS.

The origins of this likely stem from the fact that, for any given MSN n, the activity of the PYNs and TCNs projecting on n had distinct DBS-dependent patterns before each spike of n (Fig. 10 *A* and *B*). In particular, the PAN and TCN patterns were unrelated for irregular DBS (uniform distribution, Fig. 10*B*) whereas PANs and TCNs tended to fire simultaneously 8–10 ms before the neuron n under regular DBS, thus evoking concurrent depolarizing currents in n. Moreover, because the thalamo- and cortico-striatal synapses have long decay times (~10 ms, Table S1), the sum of the TCN- and PYN-evoked currents was able to combine with the antidromic effects of DBS (Fig. 8*E*), thus further increasing the depolarization of the MSNs. Overall, these results indicate that the effects of DBS on the putamen depend on the timely overlap between inputs from different pathways (reinforcement) and were maximized at the signature frequency of 130 Hz, which likely represents a resonant frequency of the overall cortico-BG-thalamo-cortical loop.

The fact that the level of entrainment of the MSNs and the level of restoration of the TCNs had a similar pattern when varying the DBS frequency and settings (Figs. 7 and 9) suggests that the projection of the MSNs onto the PANs may be relevant. To assess the impact of the striatal entrainment on the pallido-thalamic system, we simulated the network model under PD conditions and regular DBS at 130 Hz but we blocked the synaptic input from the MSNs to the GPi PANs (open-loop simulation). The lack of striatal inhibition was compensated by applying a surrogate input current $\hat{I}(t)$ to the PANs. $\hat{I}(t)$ was obtained by averaging the striato-pallidal synaptic currents over the available PANs (*SI Note 1*) and shuffling uniformly the values of this average current over time. In this way, the average level of

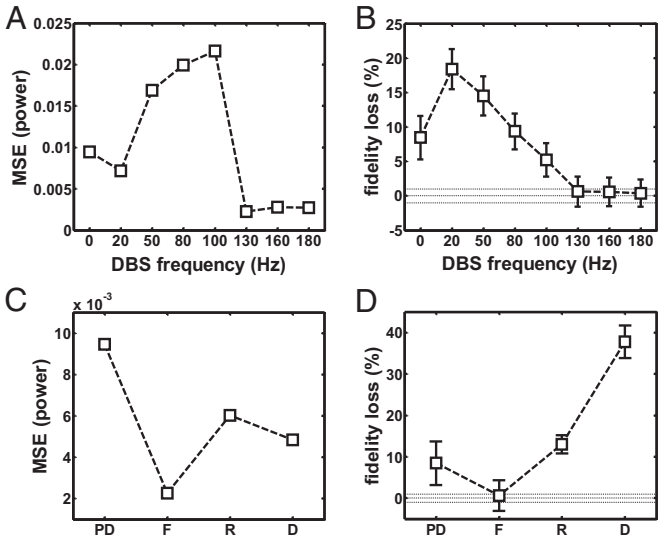

Fig. 7. (*A*) MSE in the band [3, 100] Hz between the population-average power spectrum density of the TCNs in normal and PD conditions with regular DBS vs. the DBS frequency. (*B*) Population-average loss in fidelity (mean ± SEM) of the TCNs over the value in normal conditions due to PD and regular STN DBS at several frequencies. In *A* and *B*, 0-Hz DBS means no DBS. The definition of loss in fidelity is in *SI Note 4*. (*C* and *D*) MSE in the band [3, 100] Hz (*C*) and average loss in fidelity (*D*) (mean ± SEM) of the TCNs over the value for the normal case due to PD conditions and various DBS settings. Dotted lines in *B* and *D* indicate the reference value (i.e., no increment) and 99% confidence bounds. Settings: D, PD conditions and regular 130-Hz STN DBS applied (only orthodromic effects on GPi); F, PD conditions and regular 130-Hz STN DBS applied (antidromic and orthodromic effects included); PD, PD conditions and no DBS; R, PD conditions and irregular 130-Hz STN DBS applied.

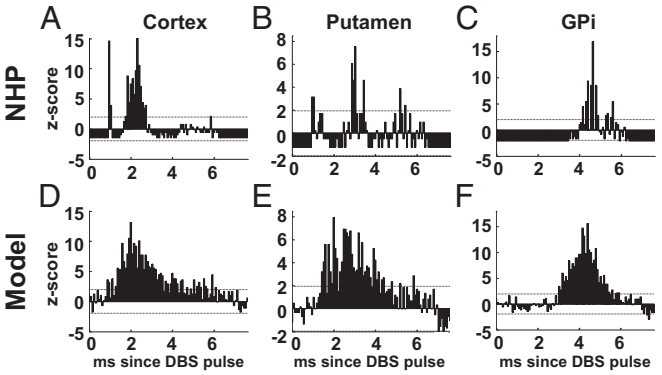

Fig. 8. PSTH (bin size: 0.08 ms) of a PYN (*A* and *D*), an MSN (*B* and *E*), and a PAN (*C* and *F*) from an MPTP-treated NHP (*A–C*) and in our model (*D–F*) under PD conditions and 130-Hz STN DBS. Dotted lines in *A–F* denote 95% confidence bounds. The single unit recordings used to compute the histograms in *A–C* are from M1 cortex, putamen, and GPi and were part of the dataset analyzed in refs. 28, 86, and 30, respectively.

inhibition provided by the MSNs to the PANs was preserved, whereas the propagation of the oscillatory pattern of the striato-pallidal input was prevented, thus assessing the impact of the closed-loop organization of the cortico-BG-thalamic system over the open-loop effects of STN DBS on the GPi neurons.

We found that, even though the average firing rate of the TCNs mildly changed because of the surrogate input to the GPi (open-loop: 12.1 ± 11.2 Hz; closed-loop: 12.4 ± 11.3 Hz), the spectral MSE of the TCNs increased by ∼10% over the value in the closed-loop simulation and, perhaps more importantly, the relay performance was significantly lower (i.e., the loss in fidelity increased by ∼200%, Fig. 10*C*).

To understand the mechanisms of this, we measured the discharge pattern of the PANs in the open-loop simulation. We found that, even though the instantaneous discharge rate of the PANs increased because of the lack of patterned GABAergic input from the MSNs (Fig. S6), the regularity of the pattern decreased, that is, the coefficient of variation [which measures the variability of the discharge pattern (33)] raised by ∼15% (Fig. 10*D*). This suggests that the pattern of the striato-pallidal input was important to maximize the restoration of the normal thalamic function.

Discussion

In the past 15 years there has been great effort to understand the effects of HFS on single neurons and neuronal populations, and to explain how these effects could relate to the restoration of movement disorders. Recordings from PD patients, MPTP-treated NHPs, and 6-OHDA–treated rats have recently shown that (*i*) the regularity of the stimulation (i.e., using constant interpulse intervals) and the high frequency are both relevant to achieve motor restoration (5, 36, 48, 81); (*ii*) STN and GPi neurons have exaggerated bursting and oscillatory firing patterns under PD conditions, which may correlate with the movement disorders (6, 52); (*iii*) HFS results into a more regular (i.e., tonic) firing of the neurons in both the stimulated site and the structures downstream from it (15, 17, 22, 23, 25, 26); and (*iv*) the measures of firing regularity (e.g., entropy, coefficient of variation, etc.) correlate with the reduction of movement disorders (22, 32, 33, 36, 49). Altogether *i–iv* led to hypothesize that the regularization of the firing patterns could be a mechanism through which motor restoration is achieved (33, 34), even though it remains elusive how HFS regularizes the firing patterns and what the effect of pattern regularization on the cortico-BG-thalamo-cortical loop is.

Computational studies (40, 41) have suggested that the pattern regularization depends on the axons projecting out of (or passing by) the stimulated site, that is, these axons may initiate action potentials at a fixed latency from the DBS pulses, thus resulting in a firing pattern that mimics the DBS pattern. This has led researchers to hypothesize that GPi and thalamocortical neurons gain more regular firing patterns because of the regularization of the presynaptic input from the STN (in case of STN HFS) and GPi (in case of GPi HFS), respectively (32–36). That is, pattern regularization is a "local" effect of HFS. However, this does not explain why the effects of stimulation would percolate to structures not directly receiving input from the stimulated axons for HFS but not for lower frequencies (24), and why, despite the fact that the regularity of the firing patterns of the stimulated axons increases with the stimulation frequency (41), the clinical benefits decrease for stimulation frequencies above 130–160 Hz (48, 49).

Our results, instead, indicate that the pattern regularization is likely a "system" effect, that is, it occurs because DBS elicits time-locked stimuli (i.e., stimuli with a fixed lag from the DBS pulse) in different structures and these stimuli eventually overlap in a gathering site (the putamen), thus causing a suprathreshold depolarization that none of them would be able to produce individually (reinforcement). The resultant regularized pattern of the striatal cells would then reenter the loop via the striato-pallidal projections and would combine with the local effects of HFS, thus sustaining itself and spreading within the GPi.

This indicates that the pattern regularization is presumably a by-product of the simultaneous occurrence of several conditions. First, it is pivotal that the cortico-BG-thalamic system forms a network of parallel, nonreciprocal, and intersecting loops (42, 62), because this lets suprathreshold DBS stimuli (which are locally applied in one structure, e.g., STN, GPi, etc.) propagate through different pathways and eventually rendezvous in a gathering site. Second, it is important that DBS elicits time-locked stimuli in the loops (41, 59) and that each loop has its own

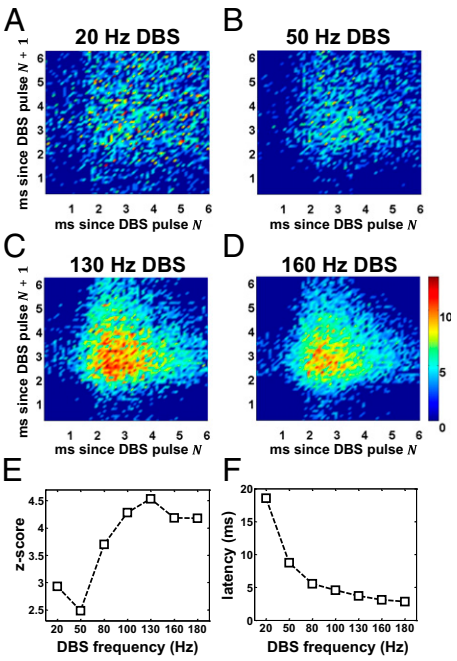

Fig. 9. (*A*–*D*) Population-average bi-PSTH (time bin: 0.1 ms) of the MSNs under PD conditions when regular STN DBS at 20 Hz (*A*), 50 Hz (*B*), 130 Hz (*C*), and 160 Hz (*D*) is applied. (*E*) Average z-score of the bi-PSTH of the MSNs over all of the pairs of latencies (x,y), with $1 < x < 5.3$ ms and $1 < y < 5.3$ ms, estimated for several DBS frequencies under PD conditions. (*F*) Population-average latency of the first poststimulus spike of the MSNs under PD conditions and STN DBS at several frequencies. Color scale in *D* also applies to *A*–*C* and indicates the z-score for each combination of poststimulus latencies. Only the z-scores above 2.58 (i.e., $P < 0.01$) are plotted.

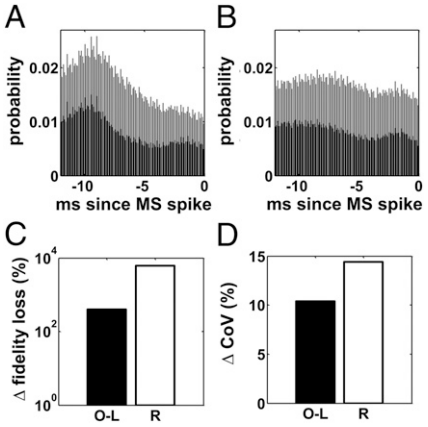

Fig. 10. (*A* and *B*) Population-average time histogram (time bin: 0.1 ms) of the TCNs (black) and PYNs (gray) projecting onto MSNs in the 12 ms preceding a spike of the target MSN (0 ms is when the spike arrives) under PD conditions when regular (*A*) and irregular (*B*) 130-Hz STN DBS is applied. (*C*) Change of average loss in fidelity of the TCNs at the transition from settings F to O-L and R, respectively. (*D*) Change of population-averaged coefficient of variation (CoV) of the PANs at the transition from settings F to O-L and R, respectively. Settings: F, PD conditions and regular 130-Hz STN DBS applied (as in Fig. 7); O-L, PD conditions and regular 130-Hz STN DBS applied, with the effects of the MSNs on the PANs blocked and replaced by a surrogate input (open-loop simulation); R, PD conditions and irregular 130-Hz STN DBS applied.

path of polysynaptic connections, because this locks the latency between any pair of stimuli passing through the gathering site (61). To clarify this point we note that a STN DBS pulse evokes an orthodromic stimulus in the GPi neurons (latency ∼3 ms) and a (perhaps antidromic) stimulus in the MSN (latency ∼2 ms), respectively (Fig. S1). The stimulus received by the GPi, though, propagates through the loop via polysynaptic connections (pallido-thalamic and thalamo-striatal synapses) and reenters the putamen. Because of the nature of these connections (synapses from GPi are GABAergic and elicit a spike in the TCN via rebound mechanisms) and the time constant of the striatal synapses, the overall time required by the orthodromic stimulus to percolate back to the putamen will be ∼17 ms. This suggests that if two consecutive DBS pulses were applied ∼15 ms apart one from one another, the stimulus due to the first pulse and propagated along the pallido-thalamo-striatal pathway would reach the putamen at the same time as the stimulus due to the second pulse that propagates straight to the MSNs, thus eliciting reinforcement. Therefore, consistently with the observations in refs. 48, 61, and 62, our simulations suggest that a regular DBS train at ∼67 Hz (i.e., the reciprocal of 15 ms), 130 Hz (reciprocal of 7.6 ms, half of 15 ms), and so on, engages this reinforcement mechanism. Note that our model is tuned on data from NHPs and 130-Hz DBS is reported as one of the most therapeutic for MPTP-treated NHPs (e.g., 5, 17, 23, 24, 26, 27, 30, 31).

The fact that reinforcement would make an impact on the whole loop only for DBS frequencies above 100 Hz instead depends on the duration of the poststimulus pattern. As reported in ref. 5, in fact, the poststimulus effects of a DBS pulse on the neuronal pattern vanish within 7–8 ms, thus letting the loop return to its abnormal prestimulus activity. Hence, 130 Hz is the first frequency for which both the reinforcement occurs and the neuronal pattern cannot turn to pre-DBS values.

Overall, these observations suggest that, even though there is a range of DBS frequencies that is likely therapeutic, there is a frequency within this range (e.g., 130 Hz in our model) that may achieve maximal restoration and that depends on the specific neural anatomy of the subject under treatment (i.e., human vs. NHP or rat).

Furthermore, because of its "system" nature, the proposed reinforcement-based mechanism is not affected by the specific location where the DBS lead is actually inserted (e.g., thalamus, STN, GPi, etc.). More precisely, because the concurrent effects of DBS on the STN, GPi, putamen, thalamus, and cortex contribute each and every one to the activation of the reinforcement, the location of the DBS lead determines which pathways are activated either orthodromically or antidromically, and hence it defines the minimum latency between consecutive pulses that allows reinforcement. This would explain why HFS of virtually every structure of the cortico-BG-thalamic system can restore at least some of the PD disorders (1–4, 43, 45, 47) and why the specific high frequency used may vary with the DBS target.

Finally, reinforcement can contribute to understanding the effect of pattern regularization on the cortico-BG-thalamo-cortical loop. The hypotheses so far [e.g., information lesion, thalamic relay restoration, etc. (33–35)] rely on the assumption that HFS must have some sort of similarity to destructive lesions. However, this hardly reconciles with the fact that there are structures (e.g., GPe) wherein applying HFS is clinically effective whereas a destructive lesion can elicit Parkinsonism (19, 47). Also, the aforementioned hypotheses are consistent with a representation of the cortico-BG-thalamo-cortical loop as a hierarchic feed-forward system where single neurons conceptually substitute for entire structures (5, 81). However, this representation is challenged by the fact that coherent frequency-specific oscillations may spread through the entire loop during Parkinsonism (52, 82) and HFS can have a decoupling effect among the various structures of the loop (51).

Our simulations, instead, suggest that the poststimulus modulation induced by HFS disrupts the ongoing firing patterns of each structure in the cortico-BG-thalamo-cortical loop (Figs. 6 *C*

and *D* and 8, and refs. 28, 30, and 31) and the disruption may facilitate the attenuation of PD-related oscillations. In the case of thalamus, the attenuation would stem from a reduced bursting activity in the pallido-thalamic subsystem and a concurrent increase of the cortico-thalamic excitation. As a result, the relay performance of the thalamocortical neurons increases despite an attenuation of the average firing rate, and the power content of the GPi neurons in the beta frequency band decreases, which is consistent with results in 6-OHDA–treated rats and MPTP-treated NHPs under HFS (51, 57).

Distal Effects of DBS Contribute to the Reinforcement. Our computational model assumes that (*i*) DBS may depolarize presynaptic terminals along with efferent axons from the stimulated site, (*ii*) this depolarization can lead to an activation of cortical, thalamic, and striatal neurons, even though with a very low probability, and (*iii*) the stimuli delivered to each neuron have a stochastic distribution.

These assumptions reflect recent evidence from computational and experimental studies. In particular, 3D reconstructions of the brain anatomy and DBS lead have been combined with multicompartment models of the neurons and fibers around the DBS electrode in refs. 54, 55, and 59, thus showing that, for therapeutic DBS amplitudes, the electric field induced by DBS in the brain can depolarize myelinated axons and passing fibers outside the stimulation target. The computational study (83) and the in vitro study (84) have also shown that the depolarization of myelinated axons and presynaptic terminals may cause antidromic action potential propagation, which can activate neurons that are upstream of the stimulated site, and numerical simulations (85) have shown that the activation of fibers of passage during STN and GPi HFS can increase the thalamic relay performance under PD conditions. Furthermore, single unit recordings in 6-OHDA–treated rats (57, 58) and MPTP-treated NHPs (28, 31, 86) have shown early (~1 ms) poststimulus spikes in cortical, striatal, and thalamic neurons during STN HFS, which is consistent with an antidromic activation of the cortico-subthalamic fibers. Finally, a count of the DBS pulses that actually result in poststimulus spikes in cortical neurons (28, 57) indicated that the efficacy of the antidromic stimuli in depolarizing neurons was generally mild.

However, little attention has been paid thus far to the therapeutic significance that these distal effects of STN HFS may have on the motor cortex, thalamus, and striatum. Our results suggest that, although limited (i.e., the probability of having a suprathreshold antidromic stimulus is small in each neuron in our model), the antidromic activation is fundamental to the reinforcement. First, the antidromic stimuli increase the rest membrane potential right after every DBS pulse, thus resulting in an increased poststimulus neuronal excitability. Second, for therapeutic HFS frequencies, this subthreshold increase of membrane potential may combine with the diffused postsynaptic depolarization caused by the orthodromic projections from motor cortex and thalamus in striatum, and this may lead to the patterned poststimulus activation of the MSNs. Finally, the recurrent subthreshold increase of the membrane potential in the cortical, striatal, and thalamic neurons tends to mask the ongoing subthreshold oscillations in the beta band, which ultimately contributes to suppress the exaggerated PD-related beta oscillations.

Interestingly, this latter point suggests that, even though the origins and the significance of the beta oscillations in the pathophysiology of Parkinsonism remain debated (52), the antidromic activation elicited by HFS might provide a contribution to the suppression of the beta oscillations by involving different structures (striatum, cortex, etc.) simultaneously. Although speculative, this spatially distributed suppression mechanism could reconcile different (and apparently conflicting) indications in refs. 57, 82, and 87–89 about which structure should be primarily targeted to suppress the beta oscillations.

Model Limitations and the Role of Other Pathways. We developed a network-based model of the cortico-BG-thalamo-cortical loop that includes populations of single-compartment neurons from the motor cortex, ventrolateral thalamus, GPi, and putamen, and we subsumed the activity of the GPe and STN in the net input to the GPi neurons. The GPe–STN subsystem has a fundamental role in the pathophysiology of PD and several studies have described the multifarious effects of DBS on the subthalamic and pallidal neurons (e.g., 12–15, 17, 22, 23, 26, 29). However, because the goals of our work were to (*i*) study the effects of DBS on a closed-loop neuronal system for several stimulation frequencies and (*ii*) understand the neuronal mechanisms of therapeutic HFS, we decided to model only a finite number of loops involving the BG, cortex, and thalamus. Furthermore, even though the GPe and STN inputs may contribute to the spontaneous activity of the GPi neurons at rest (64), it has been reported that under STN HFS, the subthalamo-pallidal projections entrain to the stimulation frequency (41), thus masking the reentrant effects of the cortex onto the STN neurons and of the striatum onto the GPe neurons. Based on these considerations, the current lack of the GPe–STN subsystem in our model has limited impact, and replacing the currently simulated net subthalamo-pallidal synaptic input to the GPi with the actual GPe–STN subsystem is expected to have minor impact on our results or even to facilitate the propagation of the reinforcement effects. In fact, there is evidence that PD-elicited exaggerated oscillations in the range of 8–30 Hz primarily affect the indirect pathway, propagate through the GPe-STN subsystem, and are attenuated in the GPe and STN by HFS (50, 72, 82). In our model, though, the input to the GPi neurons that subsumes the GPe–STN activity is not modulated by HFS, that is, our results are achieved despite the fact that we are neglecting the therapeutic effects of HFS on the indirect pathway. Furthermore, HFS has been reported to decouple the oscillatory pattern of the GPi and the STN–GPe subsystem (51), but we did not explicitly model it. It is therefore reasonable to speculate that, if the effects of HFS on the STN–GPe subsystem were modeled, the attenuation of the pathologic oscillations in the GPi would have been larger than shown in Fig. 2, and the reduction of the STN–GPe oscillatory input to the GPi would have facilitated the percolation through the direct pathway (64) (i.e., the reinforcement-driven MSN pattern would propagate toward the GPi and thalamus in a more effective way).

Another limitation in our model is the simplified representation of the motor cortex, thalamus, GPi, and putamen. Studies on single unit recordings from NHPs and PD patients have shown that different subtypes of pyramidal, thalamocortical, and pallidal neurons may have different patterns under PD conditions and DBS (76, 79, 90–92), and MSNs in the striatum may respond differently to the loss of dopamine depending on the prominent expression of D_1 or D_2 receptors (68). Our model focused on small neural populations with homogeneous properties and reproduced only a subset of the multifarious effects of Parkinson's disease and DBS. This would have little impact on the main results, though, because the mechanisms we explored primarily exploit the fact that DBS pulses modify the ongoing pattern of relevant neurons (i.e., pyramidal, thalamocortical, and medium spiny) within the cortico-BG-thalamo-cortical loop by inducing a common poststimulus response (Fig. 8) which, for these neurons, resulted independent of the specific prestimulation activity. Finally, there is evidence in NHPs and rats of GABAergic projections from the GPe to the motor striatum (93, 94). Although numerically limited, these projections have diffusive organization in the striatum and might determine a strong, DBS-locked inhibitory input to the striatal neurons, as recently proposed (95). However, because the reinforcement mechanism described above would primarily contribute to the early poststimulus activation of the MSNs along the direct pathway and because this

pallido-striatal inhibitory input would be mediated by polysynaptic connections, it is plausible that the resultant effect would not reduce the poststimulus antidromic depolarization of the MSNs. More likely, instead, this pallido-striatal input would contribute to further attenuate the exaggerated oscillations in the range of 8–30 Hz and it would account for the late poststimulus inhibition (~6–7 ms after the DBS pulse) that has been observed in striatal neurons from MPTP-treated NHPs (5, 86) and that is not entirely captured by our model.

Materials and Methods

Network Model. We developed a network of 880 single-compartment model neurons. The equations and parameters for each model neuron are as in refs. 96 (TCNs and RENs), 97 (PYNs and FSIs), 87 (PANs), and 72 (MSNs) and are reported in *SI Note 1*. The PPI model is as in ref. 98 with the ionic conductances from the soma compartment in ref. 99. The ratio of PYNs to FSIs (200:20) is as in ref. 100 and accounts for the high electrical connectivity of the cortical interneurons, which is not explicitly modeled. The ratio of MSNs to PPIs (200:20), instead, was chosen such that (*i*) the number of distinct PPIs projecting onto each MSN and (*ii*) the number of distinct MSNs reached by each PPI were as in ref. 101. Details about the network connectivity are in *SI Note 1*.

Each neuron was endowed with a constant current (I_{bias}) to simulate the background excitation and a Gaussian noise with zero mean and SD σ to simulate the subthreshold membrane voltage fluctuations (±5 mV) (Table S1). The transition from normal to PD conditions in the network model is described in *SI Note 2* and shown in Fig. S7. Briefly, we mimicked the effects of dopamine depletion on the excitability of the MSNs and PPIs in the putamen and we reproduced the altered input from the subthalamo-pallidal subsystem to the PANs in the GPi.

We simulated the effects of STN DBS on the subthalamofugal axons projecting onto the GPi by applying depolarizing current pulses to the PANs. Duration of each pulse was fixed, and the amplitude followed a Gaussian distribution and could be either supra- or subthreshold. Similarly, we simulated the antidromic effects of STN DBS on the thalamus, cortex, and putamen by applying depolarizing current pulses with normally distributed amplitudes to the TCNs, PYNs, and MSNs, respectively. See details in *SI Note 3*.

Computational Tools. The model network was simulated at room temperature (36 °C). Numerical simulations were programmed in C++ and run on a six-core Intel Xeon workstation (3.5 GHz per core). The differential equations were integrated via the midpoint method with time step 0.01 ms. Results were analyzed in MATLAB R2013a (The MathWorks, Inc.). We implemented published algorithms to compute firing and burst rates, poststimulus histograms, power spectrum densities, cross-correlation, and thalamic relay fidelity. A full description of the implementation is given in *SI Note 4*.

ACKNOWLEDGMENTS. This work was partly supported by the US National Institutes of Health (NIH) Grant R01NS073118-02, the NIH Grant 1R01NS081716-01 (to M.M.M.), the Burroughs Wellcome Fund Career Award at the Scientific Interface 1007274 (to S.V.S.), and the US National Science Foundation Career Award 1055560 (to S.V.S.).

1. The Deep-Brain Stimulation for Parkinson's Disease Study Group (2001) Deep-brain stimulation of the subthalamic nucleus or the pars interna of the globus pallidus in Parkinson's disease. *N Engl J Med* 345(13):956–963.
2. Durif F, Lemaire JJ, Debilly B, Dordain G (2002) Long-term follow-up of globus pallidus chronic stimulation in advanced Parkinson's disease. *Mov Disord* 17(4):803–807.
3. Rodriguez-Oroz MC, et al. (2005) Bilateral deep brain stimulation in Parkinson's disease: A multicentre study with 4 years follow-up. *Brain* 128(Pt 10):2240–2249.
4. Moro E, et al. (2010) Long-term results of a multicenter study on subthalamic and pallidal stimulation in Parkinson's disease. *Mov Disord* 25(5):578–586.
5. Montgomery EB, Jr, Gale JT (2008) Mechanisms of action of deep brain stimulation (DBS). *Neurosci Biobehav Rev* 32(3):388–407.
6. McIntyre CC, Hahn PJ (2010) Network perspectives on the mechanisms of deep brain stimulation. *Neurobiol Dis* 38(3):329–337.
7. Albin RL, Young AB, Penney JB (1989) The functional anatomy of basal ganglia disorders. *Trends Neurosci* 12(10):366–375.
8. DeLong MR (1990) Primate models of movement disorders of basal ganglia origin. *Trends Neurosci* 13(7):281–285.
9. Benazzouz A, et al. (2000) Effect of high-frequency stimulation of the subthalamic nucleus on the neuronal activities of the substantia nigra pars reticulata and ventrolateral nucleus of the thalamus in the rat. *Neuroscience* 99(2):289–295.
10. Dostrovsky JO, et al. (2000) Microstimulation-induced inhibition of neuronal firing in human globus pallidus. *J Neurophysiol* 84(1):570–574.
11. Kiss ZH, Mooney DM, Renaud L, Hu B (2002) Neuronal response to local electrical stimulation in rat thalamus: Physiological implications for mechanisms of deep brain stimulation. *Neuroscience* 113(1):137–143.
12. Magariños-Ascone C, Pazo JH, Macadar O, Buño W (2002) High-frequency stimulation of the subthalamic nucleus silences subthalamic neurons: A possible cellular mechanism in Parkinson's disease. *Neuroscience* 115(4):1109–1117.
13. Garcia L, Audin J, D'Alessandro G, Bioulac B, Hammond C (2003) Dual effect of high-frequency stimulation on subthalamic neuron activity. *J Neurosci* 23(25):8743–8751.
14. Filali M, Hutchison WD, Palter VN, Lozano AM, Dostrovsky JO (2004) Stimulation-induced inhibition of neuronal firing in human subthalamic nucleus. *Exp Brain Res* 156(3):274–281.
15. Meissner W, et al. (2005) Subthalamic high frequency stimulation resets subthalamic firing and reduces abnormal oscillations. *Brain* 128(Pt 10):2372–2382.
16. Anderson ME, Postupna N, Ruffo M (2003) Effects of high-frequency stimulation in the internal globus pallidus on the activity of thalamic neurons in the awake monkey. *J Neurophysiol* 89(2):1150–1160.
17. Hashimoto T, Elder CM, Okun MS, Patrick SK, Vitek JL (2003) Stimulation of the subthalamic nucleus changes the firing pattern of pallidal neurons. *J Neurosci* 23(5):1916–1923.
18. Montgomery EB, Jr (2006) Effects of GPi stimulation on human thalamic neuronal activity. *Clin Neurophysiol* 117(12):2691–2702.
19. Vitek JL, Zhang J, Hashimoto T, Russo GS, Baker KB (2012) External pallidal stimulation improves parkinsonian motor signs and modulates neuronal activity throughout the basal ganglia thalamic network. *Exp Neurol* 233(1):581–586.
20. Benabid AL (2003) Deep brain stimulation for Parkinson's disease. *Curr Opin Neurobiol* 13(6):696–706.
21. Bar-Gad I, Elias S, Vaadia E, Bergman H (2004) Complex locking rather than complete cessation of neuronal activity in the globus pallidus of a 1-methyl-4-phenyl-1,2,3,6-tetrahydropyridine-treated primate in response to pallidal microstimulation. *J Neurosci* 24(33):7410–7419.
22. Dorval AD, et al. (2008) Deep brain stimulation reduces neuronal entropy in the MPTP-primate model of Parkinson's disease. *J Neurophysiol* 100(5):2807–2818.
23. Hahn PJ, et al. (2008) Pallidal burst activity during therapeutic deep brain stimulation. *Exp Neurol* 211(1):243–251.
24. Johnson MD, Vitek JL, McIntyre CC (2009) Pallidal stimulation that improves parkinsonian motor symptoms also modulates neuronal firing patterns in primary motor cortex in the MPTP-treated monkey. *Exp Neurol* 219(1):359–362.
25. McCairn KW, Turner RS (2009) Deep brain stimulation of the globus pallidus internus in the parkinsonian primate: Local entrainment and suppression of low-frequency oscillations. *J Neurophysiol* 101(4):1941–1960.
26. McConnell GC, So RQ, Hilliard JD, Lopomo P, Grill WM (2012) Effective deep brain stimulation suppresses low-frequency network oscillations in the basal ganglia by regularizing neural firing patterns. *J Neurosci* 32(45):15657–15668.
27. Santaniello S, Gale JT, Montgomery EB, Sarma SV (2010) Modeling the motor striatum under deep brain stimulation in normal and MPTP conditions. *Conf Proc IEEE Eng Med Biol Soc* 2010:2065–2068.
28. Santaniello S, Montgomery EB, Jr, Gale JT, Sarma SV (2012) Non-stationary discharge patterns in motor cortex under subthalamic nucleus deep brain stimulation. *Front Integr Neurosci* 6:35.
29. Sarma SV, et al. (2010) Using point process models to compare neural spiking activity in the subthalamic nucleus of Parkinson's patients and a healthy primate. *IEEE Trans Biomed Eng* 57(6):1297–1305.
30. Saxena S, Santaniello S, Montgomery EB, Jr, Gale JT, Sarma SV (2010) Point process models show temporal dependencies of basal ganglia nuclei under deep brain stimulation. *Conf Proc IEEE Eng Med Biol Soc* 2010:4152–4155.
31. Xu W, Russo GS, Hashimoto T, Zhang J, Vitek JL (2008) Subthalamic nucleus stimulation modulates thalamic neuronal activity. *J Neurosci* 28(46):11916–11924.
32. Montgomery EB, Jr, Baker KB (2000) Mechanisms of deep brain stimulation and future technical developments. *Neurol Res* 22(3):259–266.
33. Grill WM, Snyder AN, Miocinovic S (2004) Deep brain stimulation creates an informational lesion of the stimulated nucleus. *Neuroreport* 15(7):1137–1140.
34. Rubin JE, Terman D (2004) High frequency stimulation of the subthalamic nucleus eliminates pathological thalamic rhythmicity in a computational model. *J Comput Neurosci* 16(3):211–235.
35. Guo Y, Rubin JE, McIntyre CC, Vitek JL, Terman D (2008) Thalamocortical relay fidelity varies across subthalamic nucleus deep brain stimulation protocols in a data-driven computational model. *J Neurophysiol* 99(3):1477–1492.
36. Dorval AD, Kuncel AM, Birdno MJ, Turner DA, Grill WM (2010) Deep brain stimulation alleviates parkinsonian bradykinesia by regularizing pallidal activity. *J Neurophysiol* 104(2):911–921.
37. Agarwal R, Sarma SV (2012) The effects of DBS patterns on basal ganglia activity and thalamic relay: A computational study. *J Comput Neurosci* 33(1):151–167.
38. Koller WC, Pahwa R, Lyons KE, Albanese A (1999) Surgical treatment of Parkinson's disease. *J Neurol Sci* 167(1):1–10.
39. Agarwal R, Sarma SV (2012) Performance limitations of relay neurons. *PLOS Comput Biol* 8(8):e1002626.
40. McIntyre CC, Grill WM (1999) Excitation of central nervous system neurons by non-uniform electric fields. *Biophys J* 76(2):878–888.
41. McIntyre CC, Grill WM, Sherman DL, Thakor NV (2004) Cellular effects of deep brain stimulation: Model-based analysis of activation and inhibition. *J Neurophysiol* 91(4):1457–1469.

42. Haber SN, Calzavara R (2009) The cortico-basal ganglia integrative network: The role of the thalamus. *Brain Res Bull* 78(2-3):69–74.
43. Canavero S, et al. (2003) Therapeutic extradural cortical stimulation for movement disorders: A review. *Neurol Res* 25(2):118–122.
44. Koller W, et al. (1997) High-frequency unilateral thalamic stimulation in the treatment of essential and parkinsonian tremor. *Ann Neurol* 42(3):292–299.
45. Montgomery EB, Jr, Huang H, Walker HC, Guthrie BL, Watts RL (2011) High-frequency deep brain stimulation of the putamen improves bradykinesia in Parkinson's disease. *Mov Disord* 26(12):2232–2238.
46. Stefani A, et al. (2007) Bilateral deep brain stimulation of the pedunculopontine and subthalamic nuclei in severe Parkinson's disease. *Brain* 130(Pt 6):1596–1607.
47. Vitek JL, Hashimoto T, Peoples J, DeLong MR, Bakay RA (2004) Acute stimulation in the external segment of the globus pallidus improves parkinsonian motor signs. *Mov Disord* 19(8):907–915.
48. Moro E, et al. (2002) The impact on Parkinson's disease of electrical parameter settings in STN stimulation. *Neurology* 59(5):706–713.
49. Kuncel AM, Cooper SE, Wolgamuth BR, Grill WM (2007) Amplitude- and frequency-dependent changes in neuronal regularity parallel changes in tremor with thalamic deep brain stimulation. *IEEE Trans Neural Syst Rehabil Eng* 15(2):190–197.
50. Kühn AA, et al. (2008) High-frequency stimulation of the subthalamic nucleus suppresses oscillatory beta activity in patients with Parkinson's disease in parallel with improvement in motor performance. *J Neurosci* 28(24):6165–6173.
51. Moran A, Stein E, Tischler H, Bar-Gad I (2012) Decoupling neuronal oscillations during subthalamic nucleus stimulation in the parkinsonian primate. *Neurobiol Dis* 45(1):583–590.
52. Stein E, Bar-Gad I (2013) Betaoscillations in the cortico-basal ganglia loop during parkinsonism. *Exp Neurol* 245:52–59.
53. Baker KB, Montgomery EB, Jr, Rezai AR, Burgess R, Lüders HO (2002) Subthalamic nucleus deep brain stimulus evoked potentials: Physiological and therapeutic implications. *Mov Disord* 17(5):969–983.
54. Butson CR, Cooper SE, Henderson JM, Wolgamuth B, McIntyre CC (2011) Probabilistic analysis of activation volumes generated during deep brain stimulation. *Neuroimage* 54(3):2096–2104.
55. Johnson MD, Zhang J, Ghosh D, McIntyre CC, Vitek JL (2012) Neural targets for relieving parkinsonian rigidity and bradykinesia with pallidal deep brain stimulation. *J Neurophysiol* 108(2):567–577.
56. Kuriakose R, et al. (2010) The nature and time course of cortical activation following subthalamic stimulation in Parkinson's disease. *Cereb Cortex* 20(8):1926–1936.
57. Li Q, et al. (2012) Therapeutic deep brain stimulation in parkinsonian rats directly influences motor cortex. *Neuron* 76(5):1030–1041.
58. Li S, Arbuthnott GW, Jutras MJ, Goldberg JA, Jaeger D (2007) Resonant antidromic cortical circuit activation as a consequence of high-frequency subthalamic deep-brain stimulation. *J Neurophysiol* 98(6):3525–3537.
59. Miocinovic S, et al. (2006) Computational analysis of subthalamic nucleus and lenticular fasciculus activation during therapeutic deep brain stimulation. *J Neurophysiol* 96(3):1569–1580.
60. Santaniello S, Gale JT, Montgomery EB, Jr, Sarma SV (2010) Modeling the effects of deep brain stimulation on sensorimotor cortex in normal and MPTP conditions. *Conf Proc IEEE Eng Med Biol Soc* 2010:2081–2084.
61. Montgomery EB, Jr (2004) Dynamically coupled, high-frequency reentrant, non-linear oscillators embedded in scale-free basal ganglia-thalamic-cortical networks mediating function and deep brain stimulation effects. *Nonlinear Studies* 11(3): 385–422.
62. Montgomery EB, Jr (2007) Basal ganglia physiology and pathophysiology: A reappraisal. *Parkinsonism Relat Disord* 13(8):455–465.
63. Sommer MA (2003) The role of the thalamus in motor control. *Curr Opin Neurobiol* 13(6):663–670.
64. Tachibana Y, Kita H, Chiken S, Takada M, Nambu A (2008) Motor cortical control of internal pallidal activity through glutamatergic and GABAergic inputs in awake monkeys. *Eur J Neurosci* 27(1):238–253.
65. Nakano K, et al. (1990) Topographical projections from the thalamus, subthalamic nucleus and pedunculopontine tegmental nucleus to the striatum in the Japanese monkey, Macaca fuscata. *Brain Res* 537(1-2):54–68.
66. Smith Y, Hazrati LN, Parent A (1990) Efferent projections of the subthalamic nucleus in the squirrel monkey as studied by the PHA-L anterograde tracing method. *J Comp Neurol* 294(2):306–323.
67. Hedreen JC, DeLong MR (1991) Organization of striatopallidal, striatonigral, and nigrostriatal projections in the macaque. *J Comp Neurol* 304(4):569–595.
68. Kreitzer AC (2009) Physiology and pharmacology of striatal neurons. *Annu Rev Neurosci* 32:127–147.
69. Bergman H, Wichmann T, Karmon B, DeLong MR (1994) The primate subthalamic nucleus. II. Neuronal activity in the MPTP model of parkinsonism. *J Neurophysiol* 72(2):507–520.
70. Raz A, Vaadia E, Bergman H (2000) Firing patterns and correlations of spontaneous discharge of pallidal neurons in the normal and the tremulous 1-methyl-4-phenyl-1,2,3,6-tetrahydropyridine vervet model of parkinsonism. *J Neurosci* 20(22): 8559–8571.
71. Soares J, et al. (2004) Role of external pallidal segment in primate parkinsonism: Comparison of the effects of 1-methyl-4-phenyl-1,2,3,6-tetrahydropyridine-induced parkinsonism and lesions of the external pallidal segment. *J Neurosci* 24(29): 6417–6426.
72. McCarthy MM, et al. (2011) Striatal origin of the pathologic beta oscillations in Parkinson's disease. *Proc Natl Acad Sci USA* 108(28):11620–11625.
73. Bevan MD, Magill PJ, Terman D, Bolam JP, Wilson CJ (2002) Move to the rhythm: Oscillations in the subthalamic nucleus-external globus pallidus network. *Trends Neurosci* 25(10):525–531.
74. Kish LJ, Palmer MR, Gerhardt GA (1999) Multiple single-unit recordings in the striatum of freely moving animals: Effects of apomorphine and D-amphetamine in normal and unilateral 6-hydroxydopamine-lesioned rats. *Brain Res* 833(1):58–70.
75. Tseng KY, Kasanetz F, Kargieman L, Riquelme LA, Murer MG (2001) Cortical slow oscillatory activity is reflected in the membrane potential and spike trains of striatal neurons in rats with chronic nigrostriatal lesions. *J Neurosci* 21(16):6430–6439.
76. Pasquereau B, Turner RS (2011) Primary motor cortex of the parkinsonian monkey: Differential effects on the spontaneous activity of pyramidal tract-type neurons. *Cereb Cortex* 21(6):1362–1378.
77. Guehl D, et al. (2003) Tremor-related activity of neurons in the 'motor' thalamus: Changes in firing rate and pattern in the MPTP vervet model of parkinsonism. *Eur J Neurosci* 17(11):2388–2400.
78. Pessiglione M, et al. (2005) Thalamic neuronal activity in dopamine-depleted primates: Evidence for a loss of functional segregation within basal ganglia circuits. *J Neurosci* 25(6):1523–1531.
79. Vitek JL, Ashe J, DeLong MR, Alexander GE (1994) Physiologic properties and somatotopic organization of the primate motor thalamus. *J Neurophysiol* 71(4): 1498–1513.
80. Shi LH, Luo F, Woodward DJ, Chang JY (2006) Basal ganglia neural responses during behaviorally effective deep brain stimulation of the subthalamic nucleus in rats performing a treadmill locomotion test. *Synapse* 59(7):445–457.
81. Montgomery EB, Jr (2005) Effect of subthalamic nucleus stimulation patterns on motor performance in Parkinson's disease. *Parkinsonism Relat Disord* 11(3):167–171.
82. Moran RJ, et al. (2011) Alterations in brain connectivity underlying beta oscillations in Parkinsonism. *PLOS Comput Biol* 7(8):e1002124.
83. Grill WM, Cantrell MB, Robertson MS (2008) Antidromic propagation of action potentials in branched axons: implications for the mechanisms of action of deep brain stimulation. *J Comput Neurosci* 24(1):81–93.
84. Chomiak T, Hu B (2007) Axonal and somatic filtering of antidromically evoked cortical excitation by simulated deep brain stimulation in rat brain. *J Physiol* 579(Pt 2): 403–412.
85. So RQ, Kent AR, Grill WM (2012) Relative contributions of local cell and passing fiber activation and silencing to changes in thalamic fidelity during deep brain stimulation and lesioning: A computational modeling study. *J Comput Neurosci* 32(3):499–519.
86. Santaniello S, Gale JT, Montgomery EB, Jr, Sarma SV (2012) Reinforcement mechanisms in putamen during high frequency STN DBS: A point process study. *Conf Proc IEEE Eng Med Biol Soc* 2012:1214–1217.
87. Hahn PJ, McIntyre CC (2010) Modeling shifts in the rate and pattern of subthalamopallidal network activity during deep brain stimulation. *J Comput Neurosci* 28(3):425–441.
88. Pedoto G, et al. (2012) Point process modeling reveals anatomical non-uniform distribution across the subthalamic nucleus in Parkinson's disease. *Conf Proc IEEE Eng Med Biol Soc* 2012:2539–2542.
89. Sarma SV, et al. (2012) The effects of cues on neurons in the basal ganglia in Parkinson's disease. *Front Integr Neurosci* 6:40.
90. Magnin M, Morel A, Jeanmonod D (2000) Single-unit analysis of the pallidum, thalamus and subthalamic nucleus in parkinsonian patients. *Neuroscience* 96(3): 549–564.
91. Molnar GF, Pilliar A, Lozano AM, Dostrovsky JO (2005) Differences in neuronal firing rates in pallidal and cerebellar receiving areas of thalamus in patients with Parkinson's disease, essential tremor, and pain. *J Neurophysiol* 93(6):3094–3101.
92. Nambu A, Llinás R (1994) Electrophysiology of globus pallidus neurons in vitro. *J Neurophysiol* 72(3):1127–1139.
93. Sato F, Lavallée P, Lévesque M, Parent A (2000) Single-axon tracing study of neurons of the external segment of the globus pallidus in primate. *J Comp Neurol* 417(1): 17–31.
94. Mallet N, et al. (2012) Dichotomous organization of the external globus pallidus. *Neuron* 74(6):1075–1086.
95. McCarthy MM, Kopell N (2013) Deep brain stimulation control of beta oscillations through the indirect pathway: A computational study. *Conf Proc Neuroscience 2013*. Abstract no. 214.16/N17. Available at www.abstractsonline.com/Plan/ViewAbstract.aspx?sKey=44517c24-47c5-4d9a-9a1b-dc63f7bdb640&cKey=bbfcae08-511e-435a-9edc-d05cb1e5a471&mKey=8d2a5bec-4825-4cd6-9439-b42bb151d1cf. Accessed January 9, 2015.
96. Destexhe A, Bal T, McCormick DA, Sejnowski TJ (1996) Ionic mechanisms underlying synchronized oscillations and propagating waves in a model of ferret thalamic slices. *J Neurophysiol* 76(3):2049–2070.
97. Destexhe A, Contreras D, Steriade M (1998) Mechanisms underlying the synchronizing action of corticothalamic feedback through inhibition of thalamic relay cells. *J Neurophysiol* 79(2):999–1016.
98. Golomb D, et al. (2007) Mechanisms of firing patterns in fast-spiking cortical interneurons. *PLOS Comput Biol* 3(8):e156.
99. Klaus A, et al. (2011) Striatal fast-spiking interneurons: From firing patterns to postsynaptic impact. *Front Syst Neurosci* 5:57.
100. McCarthy MM, Brown EN, Kopell N (2008) Potential network mechanisms mediating electroencephalographic beta rhythm changes during propofol-induced paradoxical excitation. *J Neurosci* 28(50):13488–13504.
101. Koós T, Tepper JM (1999) Inhibitory control of neostriatal projection neurons by GABAergic interneurons. *Nat Neurosci* 2(5):467–472.
102. Goldberg JA, et al. (2002) Enhanced synchrony among primary motor cortex neurons in the 1-methyl-4-phenyl-1,2,3,6-tetrahydropyridine primate model of Parkinson's disease. *J Neurosci* 22(11):4639–4653.

Supporting Information

Santaniello et al. 10.1073/pnas.1406549111

SI Note 1: Connectivity of the Network Model

Each neuron in the network model of the cortico-BG-thalamo-cortical loop (Fig. S1) received synaptic currents (AMPA-mediated glutamatergic or $GABA_a$-mediated GABAergic) from multiple neurons. Denoted with n the generic target neuron and with I_n^{pop} the net synaptic current received by neuron n from the neuronal population *pop* (i.e., one among the populations of FSIs, MSNs, PANs, PPIs, PYNs, RENs, and TCNs), we have

$$I_n^{pop} = \frac{\bar{g}_n^{type}}{N_n^{pop}} \left(\sum_{i=1}^{N_n^{pop}} s_i \right) (V_n - E_{type}), \qquad [S1]$$

where N_n^{pop} is the number of neurons in the population *pop* that project onto the neuron n, V_n is the membrane voltage (millivolts) of neuron n, $\bar{g}_n^{type}$ is the maximal conductance in neuron n for the specific type of synapses involved (AMPA or $GABA_a$), and E_{type} is the correspondent reversal potential. The gating variable s_i, $i = 1, 2, \ldots, N_n^{pop}$ describes the presynaptic release from the projecting neuron i in the population *pop* onto the neuron n, and it evolves according to the first-order differential equation (1)

$$\frac{ds_i}{dt} = \alpha \left(1 + \tanh\left(\frac{V_i}{4} \right) \right) (1 - s_i) - \frac{s_i}{\tau}, \qquad [S2]$$

where V_i is the membrane voltage (millivolts) of the neuron i, and α and τ are parameters to be assigned. For each neuron, $E_{AMPA} = 0$ mV and $E_{GABAa} = -80$ mV, and parameters α and τ were chosen for each type of neurons to match the synaptic dynamics reported in experimental studies (Table S1). In order to increase the variability of the firing patterns at rest within each population, the values $\bar{g}_n^{AMPA}$ and $\bar{g}_n^{GABAa}$ varied with the neuron n and were extracted from a Gaussian distribution with fixed mean (Table S1) and SD equal to 10% of the mean. The connectivity among the neuron models (i.e., network topology) was defined to reflect the neuronal anatomy of the cortico-BG-thalamo-cortical loop in NHPs (2–13):

Cortico-Thalamic Subsystem. The topology of this subsystem was modified from ref. 14 to reflect the dense axonal arborization and reciprocal connections between the M1 cortex and the ventrolateral thalamus (7, 11). Each PYN received AMPA-mediated synapses from 10 PYNs (nearest neighbors) and 10 TCNs (randomly chosen) and GABAergic synapses from all of the FSIs. Each FSI had synapses from all of the remaining FSIs ($GABA_a$) and PYNs (AMPA), and three randomly chosen TCNs (AMPA). Each TCN had AMPA-mediated synapses from 10 random PYNs and GABAergic synapses from eight RENs (nearest neighbors). Each REN had synapses from all of the TCNs and RENs (AMPA- and $GABA_a$-mediated, respectively) and five randomly chosen PYNs (AMPA). Each TCN also received GABAergic input from five randomly chosen PANs from the GPi to reflect the arborization of the GPi in the ventrolateral thalamus (5, 10).

Striato-Pallidal Subsystem. This subsystem included the striatal matrix compartment (15) and it explicitly modeled the convergent inputs from the cortico-thalamic system onto the putamen (4, 8, 9, 13) and the segregated projections from the putamen to the GPi (2, 3, 6). Each MSN received AMPA-mediated synapses from five PYNs and five TCNs (randomly chosen) and $GABA_a$-mediated synapses from 10 MSNs (nearest neighbors) and all of the PPIs. Each PPI had AMPA-mediated synapses from three PYNs and three TCNs (randomly chosen) and gap junctions from six PPIs (nearest neighbors). Finally, each PAN in the GPi received $GABA_a$-mediated synapses from five random MSNs.

In both subsystems, the random connections were taken from a uniform distribution. Because the connections from the PPIs to the MSNs are more than three times larger than those among MSNs (16), the maximal conductance in Eq. **S1** for the synaptic currents from the PPIs to the MSNs was set three times the value for the synaptic currents from MSNs to MSNs, and the number of PPIs projecting to each MSN was chosen as in ref. 17. Finally, the gap junction between any two PPIs was modeled as a resistive element between them (18, 19).

The combined effects of the GABAergic synapses from GPe and the glutammatergic synpases from STN onto the GPi were simulated by endowing each PAN with a stochastic sequence of depolarizing current pulses (*SI Note 2*). Furthermore, each neuron in the network received a constant current (I_{bias}) to simulate the background excitation and a Gaussian noise with zero mean and SD σ to simulate subthreshold membrane voltage fluctuations (±5 mV). Values of I_{bias} and σ for each population are reported in Table S1. Note that, for the PYNs, the value of I_{bias} was varied across the population (Gaussian distribution with mean value reported in Table S1 and SD equal to 20% of the mean) to increase the neuron-to-neuron variability of the average discharge rate, as reported in refs. 20–22.

SI Note 2: Simulation of Normal and Parkinsonian Conditions

In normal NHPs, STN and GPe neurons have weakly correlated, nonoscillatory discharge patterns (23, 24) and the striatal MSNs receive stronger inhibition from PPIs than from other MSNs (25). We captured the latter by choosing the ratio of PPIs to MSNs (20:200) and the all-to-all connection scheme between PPIs and MSNs (*SI Note 1*) consistent with histological reports (15). We simulated the effects of the STN and GPe onto the GPi, instead, by applying to each PAN a sequence of depolarizing current pulses I_S. Each PAN received a different sequence and, within each sequence, pulses were extracted from a Poisson distribution (mean and minimum interpulse interval: 20 and 10 ms, respectively), with pulse amplitudes and durations ranging in the intervals [−9.0e-3, −5.0e-4] mA/cm^2 and [5, 10] ms, respectively (uniform distribution).

The transition from normal to parkinsonian (PD) conditions was captured by simulating the effects of the loss of dopamine in the putamen and the subthalamo-pallidal subsystem. First, we lowered the baseline current I_{bias} to the MSNs (Table S1) to simulate the effect of reduced activation of the D_1 receptors, which are primarily expressed on the MSNs along the direct pathway (26). Second, we decreased by 95% the input from the PPIs to the MSNs to simulate the effects of a reduced activation of the D_5 receptors (27). Third, we simulated the effect of the increased level of acetylcholine on the M_1 receptors of the MSNs (15) by varying the maximal conductance of the M-type potassium currents, that is, for each MSN we replaced the nominal value under normal conditions [i.e., 1.3 mS/cm^2 (1)] with a random value extracted from a Gaussian distribution with mean 1.3 mS/cm^2 and SD 0.35 mS/cm^2.

Note that the reduced activation of the D_1 receptors and the acetylcholine-mediated increased activation of the M_1 receptors have opposite effects on the excitability of the MSNs (28). In our simulations, the combination of a lower current I_{bias} and

a randomized value of the M-type maximal conductance aimed to reproduce the net effect of these mechanisms combined and it guaranteed that 10–30% of the MSNs in each instance of the network model reduced the average firing rate at the transition from normal to PD conditions.

Furthermore, we accounted for the exaggerated oscillatory input that is projected from the STN and GPe onto the GPi neurons under PD conditions (23, 29, 30) by replacing the sequences I_S applied to the PANs. Specifically, we defined two classes of pulsatile sequences (class-1 and class-2) with slightly different statistical proprieties and, for each PAN, we applied either a class-1 (60% of PANs) or a class-2 (40% of PANs) sequence of current pulses I_S. Class-1 sequences were Poisson processes (mean and minimum interpulse interval: 110 and 50 ms, respectively) with pulse amplitudes and durations varying in the range [−1.3e-2, −5.0e-4] mA/cm^2 and [20, 120] ms, respectively (uniform distribution). Class-2 sequences were Poisson processes (mean and minimum interpulse interval: 40 and 20 ms, respectively), with pulse amplitudes and durations uniformly varying in [−8.0e-3, −5.0e-4] mA/cm^2 and [20, 50] ms, respectively. Class-1 and class-2 sequences reproduced a prominent 4- to 8-Hz (i.e., tremor band) and 10- to 15-Hz (i.e., beta band) oscillatory input to the GPi neurons, respectively (23), and the ratio between class-1 and class-2 recipient PANs was chosen in agreement with the proportion reported in NHPs (23). Finally, in order to increase the pairwise correlation between pallidal neurons in PD conditions (23), we applied the same stochastic sequence I_S up to 10 PANs simultaneously.

SI Note 3: Simulation of the DBS Input

STN DBS depolarizes subthalamofugal axons projecting toward the GPi (31–33). We modeled the effects of these projections on the GPi by applying depolarizing current pulses to the PANs. For each DBS pulse every PAN received a current input $I_{DBS} = A\ w_D(t-\Delta_w)$ (triangular window) with duration $D = 3$ ms, delay $\Delta_w = 2$ ms since the pulse (Fig. S2), and amplitude A extracted from a Gaussian distribution with mean μ_{DBS} and SD equal to the mean (Table S1). Amplitude A varied with each DBS pulse and neuron and could be either supra- or subthreshold. D and Δ_w accounted for the temporal dynamics of the dendritic summation of the subthalamo-pallidal inputs in the GPi somas and the synaptic propagation latency altogether, and were chosen based on experimental data (34, 35) to reproduce the poststimulus lag observed in NHPs (36).

STN DBS is also able to depolarize cortical and thalamic neurons, presumably via antidromic mechanisms (37–39), and striatal neurons, either via orthodromic activation of the subthalamo-striatal projections (4, 40) or via antidromic activation of the striatonigral projections (6, 41). We simulated the effects of STN DBS on the thalamus, cortex, and putamen by applying depolarizing current pulses to the TCNs, PYNs, and MSNs, respectively. Current pulses were modeled as for the pallidal neurons but with shorter duration (2 ms) and delay (1 ms) to match experimental data in refs. 39, 41, 42, and 43. In particular, the delay was chosen based on experimental data (44, 45) and the duration was chosen to account for potential slow-down and gating effects occurring in the soma (44, 46). Finally, the pulse amplitude varied across the pulses and neurons and it was extracted from a Gaussian distribution with mean μ_{DBS} (Table S1) and SD equal to the mean.

Regular (i.e., constant interpulse intervals) STN DBS at 20, 50, 80, 100, 130, 160, and 180 Hz was simulated in PD conditions. Two additional scenarios were simulated in case of 130-Hz STN DBS: (*i*) ineffective regular stimulation (i.e., the mean μ_{DBS} of the distributions used to generate the amplitudes A was set to 2% of the value in Table S1 for every neural population) and (*ii*) stochastic stimulation, that is, the onsets of the DBS pulses were randomly distributed according to a Gamma function with average rate 130 Hz and 60% variability, as proposed in ref. 47.

SI Note 4: Data Analysis

Rate and Burst Analysis. For each neuron under a given combination of disease condition (i.e., normal or PD) and DBS settings we computed the mean firing rate both before and during DBS as the average discharge frequency over nonoverlapping 1,000-ms-long windows. For each population the average was then computed across the available neurons (see refs. 43 and 48).

For each neuron under a given combination of disease condition and DBS settings we defined a "burst" as a group of three or more consecutive spikes, and we detected the bursts by using the modified surprise method (49). First, we identified the putative bursts as sequences of consecutive spikes whose ISIs were less than two times the mean ISI of the series. Then we refined the putative bursts by calculating the surprise index (SI) (50) for every combination of contiguous spikes and taking the combinations with the highest SI. Finally, we rejected those refined bursts that did not include at least three consecutive spikes or that had SI <3. The mean burst rate was computed as the average number of nonrejected bursts per second over nonoverlapping 3,000-ms-long windows.

Classification of Discharge Patterns. The discharge patterns of the TCNs and PYNs under normal conditions, PD conditions with no DBS applied, and PD conditions with 130-Hz DBS were classified as "regular," "random" (i.e., irregular), or "bursty" by using the criteria in ref. 21. Briefly, for every combination of disease condition and DBS settings the spike train of each neuron was divided into consecutive, nonoverlapping intervals of length Δt (Δt is the mean ISI for the train) and the number of spikes fired in each interval (i.e., spike count) was counted. Then, we computed the fraction of intervals with spike count = 0, 1, 2, 3, etc., and we constructed the correspondent histogram. Finally, we alternatively fit the histogram with a Gaussian distribution (mean = 1, SD = 0.5) and two Poisson distributions [one having mean = 1, the other one having either mean = 0.9 (cortex) or mean = 0.8 (thalamus)]. The spike train was classified as regular, random, or bursty if the best fit (in the least square sense) was given by the Gaussian distribution, Poisson distribution with mean = 1, or the other Poisson distribution, respectively.

Poststimulus Time Histograms. For each neural population and DBS settings, we computed the PSTH by counting the neuronal discharges into consecutive nonoverlapping bins (bin size = 0.1 ms) in the interstimulus intervals following each DBS pulse and normalizing to the prestimulation baseline activity (z-score). A significant ($P < 0.01$) poststimulus increase (decrease) in neuronal discharge was indicated by the PSTH at any lag from the DBS pulse when the correspondent z-score was >2.58 (< −2.58). See ref. 48 for further details.

For each DBS setting we computed the bi-PSTH for the MSNs. First, for each simulated MSN we computed the sample histogram (bin size: 0.1 ms) of the pairs (x,y), with x and y being the latencies (in milliseconds) of the first poststimulus spike within the interpulse interval for two consecutive DBS pulses. Then, we summed the histograms across the available neurons and we normalized to the prestimulation baseline activity (z-score). A significant ($P < 0.01$) poststimulus increase (decrease) in neuronal discharge activity over two consecutive DBS pulses was indicated by the bi-PSTH at any pair of lags (x,y) when the correspondent z-score was >2.58 (< −2.58).

Cross-Correlation Analysis. For each combination of neural population, disease condition, and DBS settings we computed the average pairwise cross-correlation. Briefly, we computed the cross-correlation (maximum lag: 1,000 ms) between any pair of

neurons in the neural population and we used the maximal value of the cross-correlation sequence as estimation of the cross-correlation coefficient. Then, we estimated the sample distribution of these coefficients across the available pairs of neurons in the neural population and we computed the mean and SD.

Spectral Analysis. Power spectra of individual spike trains were computed as in ref. 51. For each combination of neuron, disease condition, and DBS settings the simulated spike trains were sampled at 1,000 Hz, filtered (PYNs, TCNs, and MSNs: ninth order low-pass Butterworth filter with 1-dB cutoff at 1 Hz; PANs: ninth order band-pass Butterworth filter with 1-dB cutoffs at 5 and 20 Hz), and tampered (Hanning window). Then, the power spectrum was computed via Welch's method as the average periodogram across consecutive windows (2,000 ms per window, 500-ms overlap), thus resulting in 0.5-Hz resolution. For each population, the average spectrum across the neurons was computed and normalized to the mean power in the band [5, 40] Hz.

For the TCNs, the MSE between the population-averaged power spectrum under normal conditions ($P_{ref}(\cdot)$) and under PD conditions with DBS [$P_{DBS_x}(\cdot)$, where x is the DBS frequency, that is, $x =$ 0, 20, 50, 80, 100, 130, 160, or 180 Hz], was computed as:

$$MSE_x = \sum_{3\le f\le 100} \frac{\left(P_{DBS_x}(f) - P_{ref}(f)\right)^2}{N}, \qquad \text{[S3]}$$

where N is the number of frequency values f in the band [3, 100] Hz at which the power spectra were estimated ($N =$ 195 because of 0.5-Hz resolution). Note that the MSE was used to measure the overall distance between the power spectra of the TCNs under different conditions, whereas the interval [3, 100] Hz was chosen because the oscillatory activity of the TCNs in several bands within this interval (e.g., tremor, beta, and gamma band) is either associated with the execution of voluntary movements or affected by movement disorders (e.g., see refs. 39 and 52–57).

Relay Performance Analysis. The fidelity of the TCNs in relaying cortical inputs was defined as in refs. 58 and 59. First, we noted that each TCN receives input from 10 different PYNs simultaneously (*SI Note 1*). Second, we noted that each TCN needs the concurrent depolarization of at least 3 out of 10 presynaptic PYNs to receive a suprathreshold depolarizing synaptic current. Hence, for each TCN in a given combination of disease condition and DBS settings we computed the total number of spikes fired in consecutive, nonoverlapping time bins (1 ms per bin) by the PYNs projecting onto that TCN, and we determined the time bins wherein three or more spikes were fired concurrently. Then, we used the concurrent presence of at least three presynaptic spikes as the minimal piece of cortical information to be relayed and we assessed whether the TCN relayed it. To the purpose, we determined whether the TCN produced a "correct response" (*CR*) to each piece of information, with the *CR* occurring if the TCN spiked at least once within $\Delta r = 30$ ms since the delivery of the piece. Finally, we measured the relay fidelity of the TCN by computing the fidelity index (*FI*) (59):

$$FI = \frac{\#CR}{N_{bins}}, \qquad \text{[S4]}$$

where N_{bins} is the number of time bins with three or more concurrent cortico-thalamic inputs to that TCN. For each TCN, disease condition, and DBS settings, we computed the average *FI* value over consecutive, nonoverlapping $W =$ 3,000-ms-long windows. Variation of ±10% in the size of Δr and W did not significantly affect the results of our analysis.

We used the average *FI* (mean and SD) across all of the TCNs under normal conditions (no DBS applied) as a reference (FI_{ref}) and we compared the values of *FI* under PD conditions (either with or without DBS) to this reference. In particular, for any DBS settings under PD conditions, we computed the loss in fidelity as

$$loss = 100 \times \left| \frac{FI - \mu_{ref}}{\sigma_{ref}} \right|, \qquad \text{[S5]}$$

with μ_{ref} and σ_{ref} being the mean and SD of the reference error FI_{ref}.

SI Note 5: Population-Average Discharge Patterns and Cross-Correlation

Fig. S3 reports the population-average firing rates for the PYNs, TCNs, MSNs, and PANs in the model under different disease conditions and DBS settings (regular stimulation applied).

Fig. S4 reports the percentage of PYNs, TCNs, MSNs, and PANs under PD conditions that had significant poststimulus modulation of the discharge activity under regular DBS. In particular, we first computed the PSTH normalized to the prestimulation activity (z-score) for each neuron under 20-, 50-, and 130-Hz DBS. Then, for each DBS frequency, we analyzed the PSTHs and, for each bin (bin size: 0.1 ms), we counted how many PYNs, TCNs, MSNs, and PANs had a z-score higher than 1.96 in that bin. Finally, we plotted the percentage of neurons in each neural population having a z-score higher than 1.96 in each bin. Note that a z-score higher than 1.96 means that the likelihood of having a spike in that bin is significantly higher during stimulation than before stimulation, with a P value $P < 0.05$.

Fig. S5 assesses the direct effects of STN DBS on the poststimulus activity of PYNs and TCNs. In particular, we computed the PSTH for PYNs and TCNs under 130-Hz STN DBS for the following simulated scenarios:

i) The network model was simulated under PD conditions and the direct effects of 130-Hz DBS were applied to the PANs, PYNs, TCNs, and MSNs.
ii) The network model was simulated under PD conditions and the direct effects of 130-Hz DBS were applied to the PANs, TCNs, and MSNs, but not to the PYNs.
iii) The network model was simulated under PD conditions and the direct effects of 130-Hz DBS were applied to the PANs, PYNs, and MSNs, but not to the TCNs.

Each scenario was simulated three times (hence the number of PYNs and TCNs in Fig. S5 is $N = 600$). Fig. S5 indicates that the poststimulus activation of the neurons is primarily due to the direct effects of DBS.

For each combination of disease condition and DBS settings we estimated the cross-correlation coefficient for every pair of PANs, PYNs, TCNs, or MSNs. It resulted that, for the PYNs, the cross-correlation decreased when transitioning from normal to PD conditions and then it increased when DBS was applied (normal: 1.56e-4 ± 0.94e-4; PD with no DBS: 1.41e-4 ± 0.86e-4; PD with 130-Hz STN DBS: 3.03e-4 ± 1.26e-4; mean ± SD). The pairwise cross-correlation of the TCNs increased under PD conditions and was restored to the value for the normal state when high-frequency DBS was applied (normal: 4.15e-4 ± 3.53e-4; PD with no DBS: 5.03e-4 ± 4.19e-4; PD with 130-Hz STN DBS: 4.19e-4 ± 4.30e-4; mean ± SD). The trend for PANs and MSNs was as follows (mean ± SD):

- PANs: 4.64e-3 ± 0.19e-3 (normal); 7.26e-3 ± 0.93e-3 (PD with no DBS); 1.37e-2 ± 0.08e-2 (PD with 130-Hz STN DBS).
- MSNs: 6.0e-5 ± 2.8e-5 (normal); 1.52e-4 ± 0.95e-4 (PD with no DBS); 2.46e-4 ± 1.41e-4 (PD with 130-Hz STN DBS).

We simulated the model under PD conditions and regular 130-Hz STN DBS while blocking the synaptic currents from the MSNs to

the PANs and replacing these currents with a surrogate input (open-loop simulation; see main text for details). Then, for every PAN, we computed the firing rates in nonoverlapping 1,000-ms-long windows and we compared with the correspondent values obtained without the synaptic block from the MSNs to the PANs. Results are reported in Fig. S6.

SI Note 6: Snapshots of the Simulated Model Network

Fig. S7 reports the raster plots over a 500-ms window of the cortical neurons (PYNs and FSIs), thalamic neurons (TCNs and RENs), striatal neurons (MSNs and PPIs), and pallidal neurons (PANs) in our model network under normal conditions and PD conditions (no DBS applied), and under PD conditions with 130-Hz STN DBS (60, 61).

1. McCarthy MM, et al. (2011) Striatal origin of the pathologic beta oscillations in Parkinson's disease. *Proc Natl Acad Sci USA* 108(28):11620–11625.
2. Smith Y, Parent A (1986) Differential connections of caudate nucleus and putamen in the squirrel monkey (Saimiri sciureus). *Neuroscience* 18(2):347–371.
3. Giménez-Amaya JM, Graybiel AM (1990) Compartmental origins of the striatopallidal projection in the primate. *Neuroscience* 34(1):111–126.
4. Nakano K, et al. (1990) Topographical projections from the thalamus, subthalamic nucleus and pedunculopontine tegmental nucleus to the striatum in the Japanese monkey, Macaca fuscata. *Brain Res* 537(1-2):54–68.
5. Hazrati LN, Parent A (1991) Contralateral pallidothalamic and pallidotegmental projections in primates: An anterograde and retrograde labeling study. *Brain Res* 567(2):212–223.
6. Hedreen JC, DeLong MR (1991) Organization of striatopallidal, striatonigral, and nigrostriatal projections in the macaque. *J Comp Neurol* 304(4):569–595.
7. Rouiller EM, et al. (1998) Dual morphology and topography of the corticothalamic terminals originating from the primary, supplementary motor, and dorsal premotor cortical areas in macaque monkeys. *J Comp Neurol* 396(2):169–185.
8. McFarland NR, Haber SN (2000) Convergent inputs from thalamic motor nuclei and frontal cortical areas to the dorsal striatum in the primate. *J Neurosci* 20(10): 3798–3813.
9. McFarland NR, Haber SN (2001) Organization of thalamostriatal terminals from the ventral motor nuclei in the macaque. *J Comp Neurol* 429(2):321–336.
10. Parent M, Lévesque M, Parent A (2001) Two types of projection neurons in the internal pallidum of primates: Single-axon tracing and three-dimensional reconstruction. *J Comp Neurol* 439(2):162–175.
11. McFarland NR, Haber SN (2002) Thalamic relay nuclei of the basal ganglia form both reciprocal and nonreciprocal cortical connections, linking multiple frontal cortical areas. *J Neurosci* 22(18):8117–8132.
12. Shepherd GM (2004) *The Synaptic Organization of the Brain* (Oxford Univ Press, New York).
13. Parent M, Parent A (2006) Single-axon tracing study of corticostriatal projections arising from primary motor cortex in primates. *J Comp Neurol* 496(2):202–213.
14. Destexhe A, Contreras D, Steriade M (1998) Mechanisms underlying the synchronizing action of corticothalamic feedback through inhibition of thalamic relay cells. *J Neurophysiol* 79(2):999–1016.
15. Kreitzer AC (2009) Physiology and pharmacology of striatal neurons. *Annu Rev Neurosci* 32:127–147.
16. Planert H, Szydlowski SN, Hjorth JJ, Grillner S, Silberberg G (2010) Dynamics of synaptic transmission between fast-spiking interneurons and striatal projection neurons of the direct and indirect pathways. *J Neurosci* 30(9):3499–3507.
17. Koós T, Tepper JM (1999) Inhibitory control of neostriatal projection neurons by GABAergic interneurons. *Nat Neurosci* 2(5):467–472.
18. Hjorth J, Blackwell KT, Kotaleski JH (2009) Gap junctions between striatal fast-spiking interneurons regulate spiking activity and synchronization as a function of cortical activity. *J Neurosci* 29(16):5276–5286.
19. Klaus A, et al. (2011) Striatal fast-spiking interneurons: From firing patterns to postsynaptic impact. *Front Syst Neurosci* 5:57.
20. Goldberg JA, et al. (2002) Enhanced synchrony among primary motor cortex neurons in the 1-methyl-4-phenyl-1,2,3,6-tetrahydropyridine primate model of Parkinson's disease. *J Neurosci* 22(11):4639–4653.
21. Pasquereau B, Turner RS (2011) Primary motor cortex of the parkinsonian monkey: Differential effects on the spontaneous activity of pyramidal tract-type neurons. *Cereb Cortex* 21(6):1362–1378.
22. Pessiglione M, et al. (2005) Thalamic neuronal activity in dopamine-depleted primates: Evidence for a loss of functional segregation within basal ganglia circuits. *J Neurosci* 25(6):1523–1531.
23. Raz A, Vaadia E, Bergman H (2000) Firing patterns and correlations of spontaneous discharge of pallidal neurons in the normal and the tremulous 1-methyl-4-phenyl-1,2,3,6-tetrahydropyridine vervet model of parkinsonism. *J Neurosci* 20(22):8559–8571.
24. Wichmann T, Bergman H, DeLong MR (1994) The primate subthalamic nucleus. I. Functional properties in intact animals. *J Neurophysiol* 72(2):494–506.
25. Koós T, Tepper JM, Wilson CJ (2004) Comparison of IPSCs evoked by spiny and fast-spiking neurons in the neostriatum. *J Neurosci* 24(36):7916–7922.
26. Ince E, Ciliax BJ, Levey AI (1997) Differential expression of D1 and D2 dopamine and m4 muscarinic acetylcholine receptor proteins in identified striatonigral neurons. *Synapse* 27(4):357–366.
27. Centonze D, et al. (2003) Receptor subtypes involved in the presynaptic and postsynaptic actions of dopamine on striatal interneurons. *J Neurosci* 23(15):6245–6254.
28. Mallet N, Ballion B, Le Moine C, Gonon F (2006) Cortical inputs and GABA interneurons imbalance projection neurons in the striatum of parkinsonian rats. *J Neurosci* 26(14):3875–3884.
29. Bergman H, Wichmann T, Karmon B, DeLong MR (1994) The primate subthalamic nucleus. II. Neuronal activity in the MPTP model of parkinsonism. *J Neurophysiol* 72(2):507–520.
30. Wichmann T, Bergman H, DeLong MR (1994) The primate subthalamic nucleus. III. Changes in motor behavior and neuronal activity in the internal pallidum induced by subthalamic inactivation in the MPTP model of parkinsonism. *J Neurophysiol* 72(2): 521–530.
31. McIntyre CC, Grill WM (1999) Excitation of central nervous system neurons by nonuniform electric fields. *Biophys J* 76(2):878–888.
32. McIntyre CC, Grill WM, Sherman DL, Thakor NV (2004) Cellular effects of deep brain stimulation: Model-based analysis of activation and inhibition. *J Neurophysiol* 91(4):1457–1469.
33. Miocinovic S, et al. (2006) Computational analysis of subthalamic nucleus and lenticular fasciculus activation during therapeutic deep brain stimulation. *J Neurophysiol* 96(3):1569–1580.
34. Hanson JE, Smith Y, Jaeger D (2004) Sodium channels and dendritic spike initiation at excitatory synapses in globus pallidus neurons. *J Neurosci* 24(2):329–340.
35. Jaeger D, Kita H (2011) Functional connectivity and integrative properties of globus pallidus neurons. *Neuroscience* 198:44–53.
36. Saxena S, Santaniello S, Montgomery EB, Jr, Gale JT, Sarma SV (2010) Point process models show temporal dependencies of basal ganglia nuclei under deep brain stimulation. *Conf Proc IEEE Eng Med Biol Soc* 2010:4152–4155.
37. Li Q, et al. (2012) Therapeutic deep brain stimulation in parkinsonian rats directly influences motor cortex. *Neuron* 76(5):1030–1041.
38. Li S, Arbuthnott GW, Jutras MJ, Goldberg JA, Jaeger D (2007) Resonant antidromic cortical circuit activation as a consequence of high-frequency subthalamic deep-brain stimulation. *J Neurophysiol* 98(6):3525–3537.
39. Xu W, Russo GS, Hashimoto T, Zhang J, Vitek JL (2008) Subthalamic nucleus stimulation modulates thalamic neuronal activity. *J Neurosci* 28(46):11916–11924.
40. Smith Y, Hazrati LN, Parent A (1990) Efferent projections of the subthalamic nucleus in the squirrel monkey as studied by the PHA-L anterograde tracing method. *J Comp Neurol* 294(2):306–323.
41. Montgomery EB, Jr, Gale JT (2008) Mechanisms of action of deep brain stimulation (DBS). *Neurosci Biobehav Rev* 32(3):388–407.
42. Santaniello S, Gale JT, Montgomery EB, Jr, Sarma SV (2012) Reinforcement mechanisms in putamen during high frequency STN DBS: A point process study. *Conf Proc IEEE Eng Med Biol Soc* 2012:1214–1217.
43. Santaniello S, Montgomery EB, Jr, Gale JT, Sarma SV (2012) Non-stationary discharge patterns in motor cortex under subthalamic nucleus deep brain stimulation. *Front Integr Neurosci* 6:35.
44. Chomiak T, Hu B (2007) Axonal and somatic filtering of antidromically evoked cortical excitation by simulated deep brain stimulation in rat brain. *J Physiol* 579(Pt 2): 403–412.
45. Walker HC, et al. (2012) Short latency activation of cortex during clinically effective subthalamic deep brain stimulation for Parkinson's disease. *Mov Disord* 27(7):864–873.
46. Grill WM, Cantrell MB, Robertson MS (2008) Antidromic propagation of action potentials in branched axons: implications for the mechanisms of action of deep brain stimulation. *J Comput Neurosci* 24(1):81–93.
47. Dorval AD, Kuncel AM, Birdno MJ, Turner DA, Grill WM (2010) Deep brain stimulation alleviates parkinsonian bradykinesia by regularizing pallidal activity. *J Neurophysiol* 104(2):911–921.
48. Montgomery EB, Jr (2006) Effects of GPi stimulation on human thalamic neuronal activity. *Clin Neurophysiol* 117(12):2691–2702.
49. Hahn PJ, et al. (2008) Pallidal burst activity during therapeutic deep brain stimulation. *Exp Neurol* 211(1):243–251.
50. Legéndy CR, Salcman M (1985) Bursts and recurrences of bursts in the spike trains of spontaneously active striate cortex neurons. *J Neurophysiol* 53(4):926–939.
51. Moran A, Stein E, Tischler H, Bar-Gad I (2012) Decoupling neuronal oscillations during subthalamic nucleus stimulation in the parkinsonian primate. *Neurobiol Dis* 45(1): 583–590.
52. Jenkinson N, Kühn AA, Brown P (2013) Gamma oscillations in the human basal ganglia. *Exp Neurol* 245:72–76.
53. Ribary U (2005) Dynamics of thalamo-cortical network oscillations and human perception. *Prog Brain Res* 150:127–142.
54. Lenz FA, et al. (1990) Single unit analysis of the human ventral thalamic nuclear group. Activity correlated with movement. *Brain* 113(Pt 6):1795–1821.
55. Lenz FA, et al. (1994) Single unit analysis of the human ventral thalamic nuclear group. Tremor-related activity in functionally identified cells. *Brain* 117(Pt 3):531–543.
56. Lenz FA, et al. (1988) Single unit analysis of the human ventral thalamic nuclear group: Correlation of thalamic "tremor cells" with the 3-6 Hz component of parkinsonian tremor. *J Neurosci* 8(3):754–764.
57. Zirh TA, Lenz FA, Reich SG, Dougherty PM (1998) Patterns of bursting occurring in thalamic cells during parkinsonian tremor. *Neuroscience* 83(1):107–121.
58. Guo Y, Rubin JE, McIntyre CC, Vitek JL, Terman D (2008) Thalamocortical relay fidelity varies across subthalamic nucleus deep brain stimulation protocols in a data-driven computational model. *J Neurophysiol* 99(3):1477–1492.
59. Agarwal R, Sarma SV (2012) Performance limitations of relay neurons. *PLOS Comput Biol* 8(8):e1002626.
60. Destexhe A, Bal T, McCormick DA, Sejnowski TJ (1996) Ionic mechanisms underlying synchronized oscillations and propagating waves in a model of ferret thalamic slices. *J Neurophysiol* 76(3):2049–2070.
61. Chuhma N, Tanaka KF, Hen R, Rayport S (2011) Functional connectome of the striatal medium spiny neuron. *J Neurosci* 31(4):1183–1192.

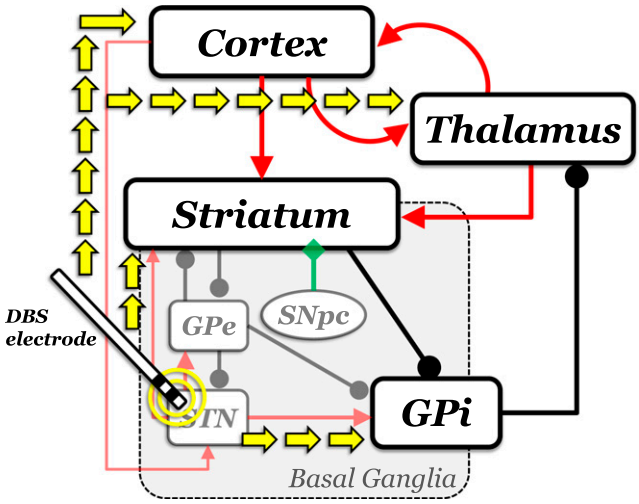

Fig. S1. Schematic of the cortico-BG-thalamo-cortical loop with the direct effects of STN DBS on cortex, striatum, GPi, and thalamus (yellow arrows). Red, black, and green arrows are glutamatergic, GABAergic, and dopaminergic projections, respectively. The structures explicitly modeled are depicted with black boxes, and the remaining structures are in gray boxes. Legend: GPe (GPi), external (internal) globus pallidus; SNpc, substantia nigra pars compacta; STN, subthalamic nucleus.

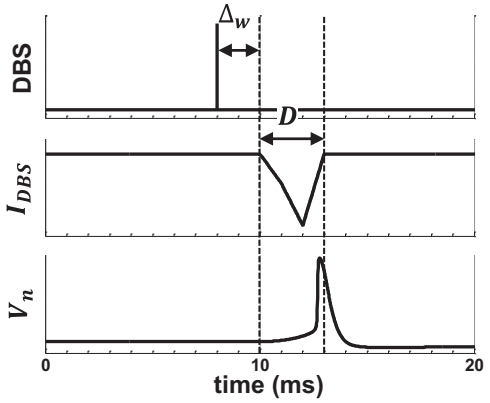

Fig. S2. Schematic of the simulation of the effects of a STN DBS pulse onto a GPi neuron. When the DBS pulse is delivered (*Top*), a delayed poststimulus current (I_{DBS}) is applied to the neuron, where the delay Δ_W and the duration D of the current mimic the propagation of the pulse from the STN to the presynaptic area of the neuron and the postsynaptic inflow, respectively. If I_{DBS} is suprathreshold, the membrane potential V_n of the neuron results in an action potential.

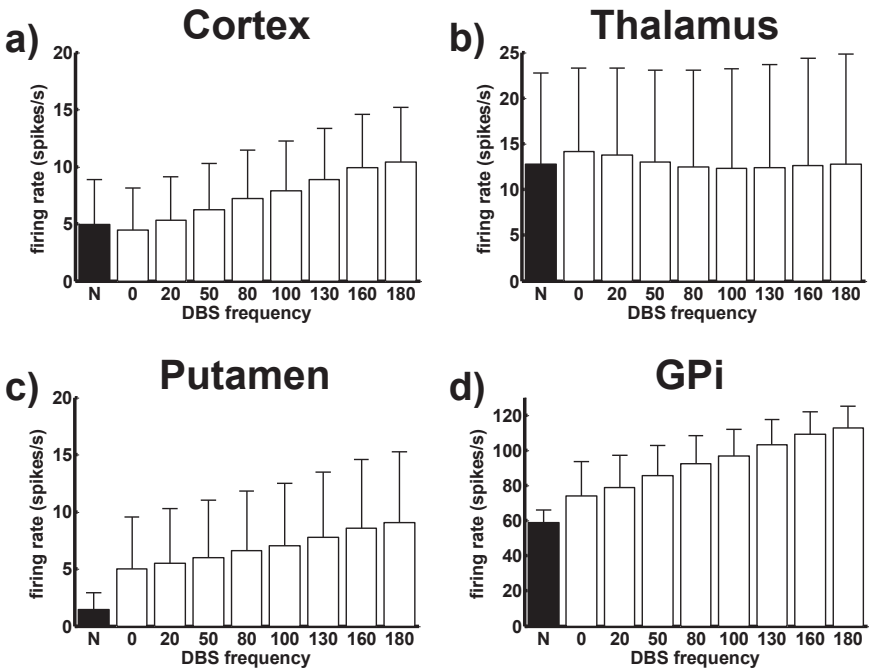

Fig. S3. Population-average firing rate (mean + SD) of PYNs (*A*), TCNs (*B*), MSNs (*C*), and PANs (*D*) in normal conditions at rest (N) and in PD conditions with regular DBS applied at several frequencies. Each population includes $N = 600$ neurons. 0-Hz DBS means no stimulation applied.

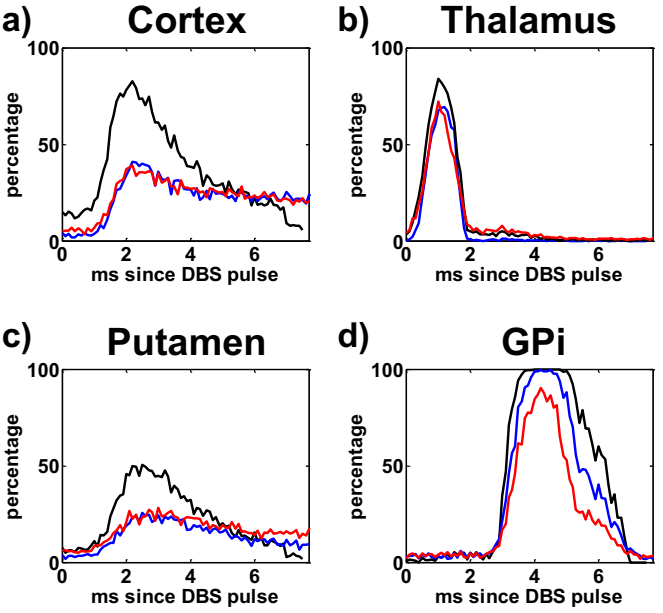

Fig. S4. Percentages of PYNs (*A*), TCNs (*B*), MSNs (*C*), and PANs (*D*) simulated under PD conditions whose PSTH has a z-score higher than 1.96 when DBS at 20 Hz (red lines), 50 Hz (blue lines), and 130 Hz (black lines) is applied. Each population includes $N = 600$ neurons.

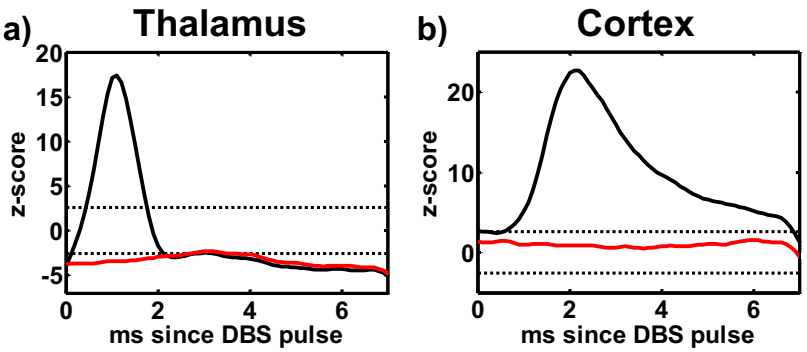

Fig. S5. PSTH (bin width: 0.2 ms) of TCNs (*A*) and PYNs (*B*) estimated under PD conditions with 130-Hz STN DBS. Black lines are computed for scenario *i* in *SI Note 5*. Red lines are computed for scenarios *iii* and *ii* in *SI Note 5*, respectively. Black dotted lines denote the 95% confidence bounds.

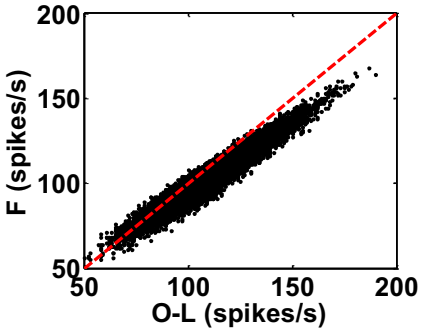

Fig. S6. Each dot reports the discharge rate of a PAN ($N = 600$ neurons) in a nonoverlapping 1,000-ms-long window for two DBS settings, i.e., F (*y* axis) and O-L (*x* axis). Settings: F, PD conditions and regular 130-Hz STN DBS applied (antidromic and orthodromic effects included); O-L, as settings F but the synaptic currents from the MSNs to the PANs are blocked and replaced by a surrogate input (open-loop simulation).

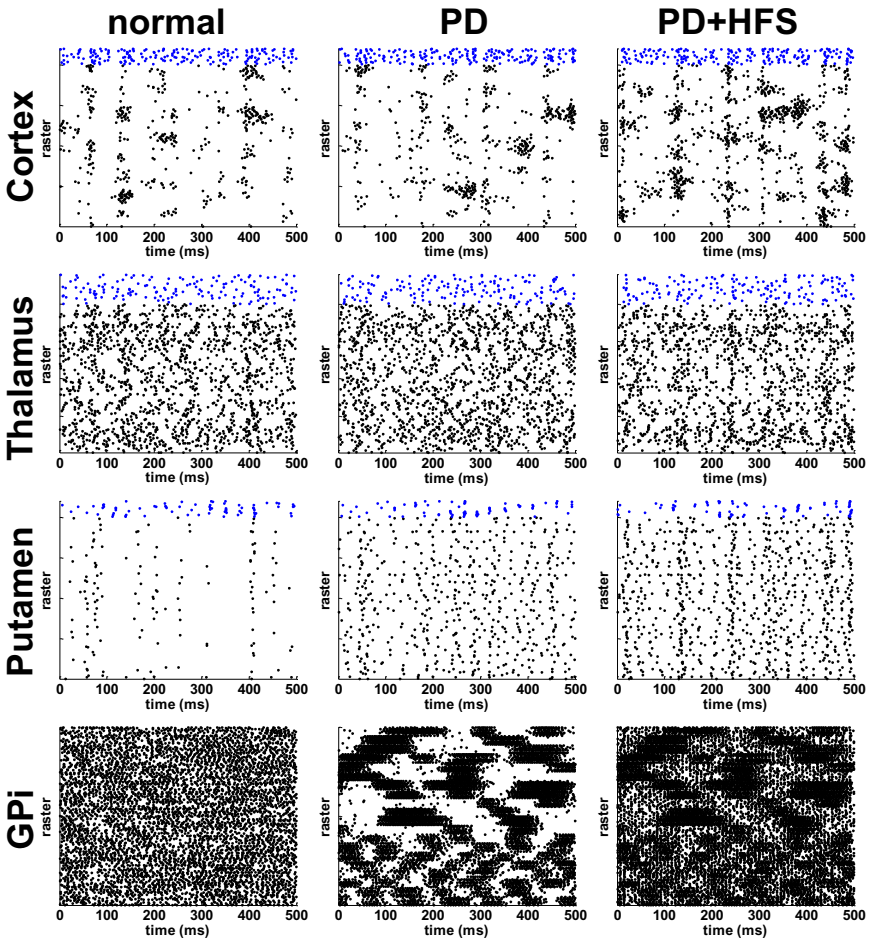

Fig. S7. Raster plot of the simulated model neurons under normal conditions (left column), PD conditions with no stimulation (center column), and PD conditions with 130-Hz STN DBS (PD+HFS, left column). From top to bottom: PYNs (black dots) and FSIs (blue dots) in the cortex; TCNs (black dots) and RENs (blue dots) in the thalamus; MSNs (black dots) and PPIs (blue dots) in the putamen; PANs in the GPi.

Table S1. Parameters in the model

Neuron type	I_{bias}, mA/cm^2	μ_{DBS}, mA/cm^2	σ Gaussian noise, mA/cm^2	$\langle \bar{g}_{type} \rangle$, S/cm^2	Synaptic gate s	Refs.
PYN	−1.88e-3	−3.5e-3	−1.0e-3	2.7e-4 (AMPA) 3.6e-4 ($GABA_a$)	To PYNs, FSIs, TCNs RENs: $\alpha = 0.55$; $\tau = 5.26$ ms To MSNs: $\alpha = 0.2$; $\tau = 16.7$ ms To PPIs: $\alpha = 0.23$; $\tau = 2.38$ ms	14 18 16, 19
FSI	−2.0e-3	NA	−1.0e-3	2.9e-4 (AMPA) 1.0e-4 ($GABA_a$)	To PYNs, FSIs: $\alpha = 2.5$; $\tau = 5.56$ ms	14
TCN	−3.0e-3	−4.0e-3	−7.0e-4	3.7e-4 (AMPA) 1.6e-4 ($GABA_a$)	To PYNs, FSIs, RENs: $\alpha = 0.55$; $\tau = 5.26$ ms To MSNs: $\alpha = 0.2$; $\tau = 11.1$ ms To PPIs: $\alpha = 0.23$; $\tau = 2.38$ ms	14 18 16, 19
REN	−1.0e-3	NA	−7.0e-4	1.0e-4 (AMPA) 8.0e-4 ($GABA_a$)	To RENs, TCNs: $\alpha = 10$; $\tau = 6.17$ ms	60
MSN	−5.0e-4* −3.5e-4**	−1.7e-3	−7.0e-4	1.3e-4 (AMPA) 3.5e-4 ($GABA_a$)† 1.0e-3 ($GABA_a$)§	To MSNs, PANs: $\alpha = 2.0$; $\tau = 13.0$ ms	1
PPI	−3.0e-3	NA	−1.0e-3	1.0e-4 (AMPA) 2.0e-4 ($GABA_a$)	To MSNs: $\alpha = 2.0$; $\tau = 13.0$ ms	61
PAN	NA	−4.3e-3	−1.0e-3	3.4e-4 ($GABA_a$)	To TCNs: $\alpha = 10$; $\tau = 6.17$ ms	60

$\langle \bar{g}_{type} \rangle$, mean value of the maximal conductance ("type" is either AMPA or $GABA_a$) in the neurons of the type specified in the first column; s, gating variable in Eq. **S2** from the neurons of the type specified in the first column. For each type of target neuron, α and τ are reported along with the correspondent reference (last column). †Synapses from MSNs; §synapses from PPIs; *normal state; **PD state; NA, not applied. Note that I_{bias} is the average value in case of PYNs.